

Deformation mechanisms in mafic amphibolites and granulites: record from the Semail metamorphic sole during subduction infancy

Mathieu Soret¹, Philippe Agard¹, Benoît Ildefonse², Benoît Dubacq¹, Cécile Prigent³, Claudio Rosenberg¹

¹ Sorbonne Université, CNRS-INSU, Institut des Sciences de la Terre Paris, ISTE^P UMR 7193, F-75005 Paris, France

⁵ ² Géosciences Montpellier, Univ. Montpellier, CNRS, Univ. Antilles, 34095, Montpellier, cedex, 05, France

³ Univ. Grenoble Alpes, Univ. Savoie Mont Blanc, CNRS, IRD, IFSTTAR, ISTerre, 38000 Grenoble, France

Correspondence to: Mathieu Soret (math.soret@gmail.com)

Abstract. This study sheds light on the deformation mechanisms of subducted mafic rocks metamorphosed at amphibolite and granulite facies conditions, and on their importance for strain accommodation and localization at the top of the slab during 10 subduction infancy. These rocks, namely metamorphic soles, are oceanic slivers stripped from the downgoing slab and accreted below the upper plate mantle wedge during the first million years of intra-oceanic subduction, when the subduction interface is still warm. Their formation and intense deformation (i.e. shear strain ≥ 5) attest to a systematic and transient coupling between the plates over a restricted time span of ~ 1 My and specific rheological conditions. Combining micro-structural analyses with mineral chemistry constrains grain-scale deformation mechanisms and the rheology of amphibole and 15 amphibolites along the plate interface during early subduction dynamics, as well as the interplay between brittle and ductile deformation, water activity, mineral change, grain size reduction and phase mixing.

Results indicate that increasing pressure-temperature conditions and slab dehydration (from amphibolite to granulite facies) lead to the nucleation of mechanically strong phases (garnet, clinopyroxene and amphibole) and rock hardening. Peak 20 conditions (850°C and 1 GPa) coincide with a pervasive stage of brittle deformation which enables strain localization in the top of the mafic slab and therefore possibly the unit detachment from the slab. In contrast, during early exhumation and cooling (from ~ 850 down to $\sim 700^\circ\text{C}$ and 0.7 GPa), the garnet-clinopyroxene-bearing amphibolite experiences extensive retrogression (and fluid ingress) and significant strain weakening essentially accommodated in the dissolution-precipitation creep regime including heterogeneous nucleation of fine-grained materials and the activation of grain boundary sliding processes. This 25 deformation mechanism is closely assisted with continuous fluid-driven fracturing throughout the exhumed amphibolite, which contributes to fluid channelization within the amphibolites. These mechanical transitions, coeval with detachment and early exhumation of the HT metamorphic soles, controlled therefore the viscosity contrast and mechanical coupling across the plate interface during subduction infancy, between the top of the slab and the overlying peridotites. Our findings may thus apply to other geodynamic environments where similar temperatures, lithologies, fluid circulation and mechanical coupling between mafic rocks and peridotites prevail, such as in mature warm subduction zones (e.g., Nankai, Cascadia), in lower continental 30 crust shear zones and oceanic detachments.

1 Introduction

Metamorphic soles underlying ophiolites are 10–100 m thick metamorphosed oceanic slivers stripped from the slab during subduction infancy (Hacker, 1990; Dewey and Casey, 2013; Agard et al., 2016; Rioux et al., 2016; Guilmette et al., 2018). Their accretion to the upper plate mantle wedge (i.e., the future ophiolite; Fig. 1a) is indicative of the rheology of the nascent, 5 still warm interface, which favours strong mechanical coupling between the two plates (Agard et al., 2016, 2018; Soret et al., 2016, 2017). Internal changes in lithologies and metamorphic conditions reveal short-lived, stepwise accretion at characteristic pressure-temperature-time (P–T–t) conditions (Wakabayashi and Dilek, 2000, 2003; Plunder et al., 2016; Soret et al., 2017): two major accretion events have been identified in the mafic, high-temperature amphibolite to granulite facies portions of the 10 Semail ophiolite sole (Oman, and United Arab Emirates; UAE), at $850 \pm 50^\circ\text{C}$ and $0.9 \pm 0.2 \text{ GPa}$ and $750 \pm 50^\circ\text{C}$ and $0.7 \pm 0.2 \text{ GPa}$ (Soret et al., 2017). The striking similarity of P–T conditions across the whole ophiolite width ($\sim 150 \text{ km}$) also indicates that these slivers experienced shear strains of at least 4–5 gamma during accretion/exhumation (Soret et al., 2017), coeval with 15 large ductile deformation in the banded peridotites above (Boudier et al., 1988; Prigent et al., 2018a,c).

How deformation is accommodated within the amphibole-bearing sole rocks, and how mafic slivers get detached from the top of the subducting slab and accreted to the upper plate at $T \geq 700^\circ\text{C}$ is so far unknown. To investigate the deformation 15 mechanisms accompanying the progressive change of P–T conditions and mineralogy (i.e., essentially amphibole, with varying amounts of plagioclase, clinopyroxene and garnet), we provide detailed micro-structural and mineral chemistry data from the well-constrained Semail ophiolite sole. In contrast to plagioclase and clinopyroxene (e.g., Bascou et al., 2002; Rybacki and Dresen, 2004; Hier-Majumder et al., 2005; Dimanov et al., 2007), the physical properties and mechanical behaviour of 20 amphibole and amphibole-bearing polymimetic aggregates, commonly found over a large range of P–T and water activity conditions, have been far less studied and remain puzzling (see Getsinger and Hirth, 2014). Understanding their deformation mechanisms is therefore expected to shed light on the plate interface rheology during subduction infancy (Soret et al., 2016, 2017; Prigent et al., 2018b) or beneath warm subduction zones (where similar temperatures, lithologies and mechanical 25 coupling are expected at $\sim 60 \text{ km}$ depth; Abers et al., 2017), as well as on the rheological behaviour of amphibole-bearing rocks and strain localization in mid-crustal environments (e.g., continental crust: Imon et al., 2004; Tatham et al., 2008; Getsinger et al., 2013; Giuntoli et al., 2018; oceanic detachment faults or transform faults: Boschi et al., 2006; Escartín et al., 2003).

2 Deformation of amphibolites

Naturally and experimentally deformed amphibolites commonly show well-developed foliation and strong crystallographic–preferred orientation (CPO), regardless of their P–T–water activity conditions and compositional range (e.g., Imon et al., 2004; Tatham et al., 2008; Cao et al., 2010; Getsinger et al., 2013; Ko and Jung, 2015; Marti et al., 2017, 2018; Giuntoli et al., 2018). 30 Foliation is usually underlined by the shape–preferred orientations (SPO) of amphibole and plagioclase. Compared to plagioclase and clinopyroxene, the CPO of amphibole is generally stronger (Siegesmund et al., 1994; Imon et al., 2004; Diaz

Aspiroz et al., 2007; Tatham et al., 2008; Cao et al., 2010; Gómez Barreiro et al., 2010; Getsinger et al., 2013; Getsinger and Hirth, 2014; Kim et al., 2015; Ko and Jung, 2015), hence leading several authors to consider that it accounts for seismic anisotropy in the lower/middle crust (Mainprice and Nicolas, 1989; Tatham et al., 2008; Lloyd et al., 2011; Ji et al., 2013) and in subduction zones (Ko and Jung, 2015).

5 There are different interpretations for the strong CPO of amphibole and its SPO. The presence of a CPO usually hints at dislocation creep as the dominant deformation mechanism (e.g., Wenk and Christie, 1991). Several studies report intra-crystalline deformation in amphibole at high temperature ($T \geq 650\text{--}700^\circ\text{C}$), compatible with dislocation glide along the most favourable slip systems $\{hk0\}[001]$ (Berger and Stünitz, 1996; Diaz Aspiroz et al., 2007; Cao et al., 2010; Gomez Barreiro et al., 2010). However, other studies have suggested that amphibole is one of the strongest silicates, with limited ability to deform 10 by dislocation creep (e.g., Brodie and Rutter, 1985). Amphibole would rather behave as a rigid particle, rotating and fracturing (Hacker and Christie, 1990; Ildefonse et al., 1990; Nyman et al., 1992; Shelley, 1994; Berger and Stünitz, 1996; Imon et al., 2004; Ko and Jung, 2015), and/or dissolving and reprecipitating during deformation (Brodie, 1981; Hacker and Christie, 1990; Berger and Stünitz, 1996; Kruse et al., 1999; Imon et al., 2004; Marti et al., 2017, 2018; Guintoli et al., 2018). While variations 15 in P–T conditions, water activity and grain size are known to control the activation of the different deformation mechanisms (e.g., Brodie and Rutter, 1985), their respective roles have not been clearly assessed in the specific case of amphibole.

3 The Semail metamorphic sole

The Semail metamorphic sole is a relatively thin unit (commonly ≤ 100 m thick) found at the base of the ≥ 10 km thick Semail ophiolite (Oman and UAE; Fig. 1a-c). This unit results from the juxtaposition of several slices of oceanic crust (Fig. 1c-d; Soret et al., 2017 and references therein) that were buried, strained and metamorphosed against the hot overlying mantle wedge,

20 from granulite-facies (for the uppermost slice) to upper greenschist facies conditions (for the lowermost one). In practice, it is convenient to distinguish in the field a high-temperature (HT) sole, found directly below the mylonitic basal peridotite, from a low-temperature (LT) sole onto which the HT sole is thrust. This structural organization is found all along the Semail ophiolite (Fig. 1b-c; Gnos, 1998), from Wadi Tayin (Oman) in the south to Sumeini (Oman) and Asimah–Khubakhib (UAE) in the north. These characteristics are common to most metamorphic soles worldwide, regardless of the nature of the overlying 25 ophiolite (see Agard et al., 2016).

The HT sole is composed of two major sub-units (Fig. 1c), being either made of garnet–clinopyroxene amphibolites (HTa, above) or plagioclase-rich amphibolites (HTb, below). The contrasting Ti content of amphibole, which correlates positively with crystallization temperature (Ernst and Liu, 1998) and shows a stepwise decrease from ≥ 0.2 a.p.f.u. (atoms per formula unit) in HTa to ≤ 0.15 a.p.f.u. in HTb (Fig. 1e; Soret et al., 2017), indicates a $\sim 100^\circ\text{C}$ gap in peak T between the two units.

30 Mapping of the Ti-content is used hereafter to track different amphibole generations (Sect. 5.3).

Peak P–T conditions for the HT sole were estimated at $850 \pm 50^\circ\text{C}$ and $0.9 \pm 0.1 \text{ GPa}$ for HTa and $725 \pm 50^\circ\text{C}$ and $0.8 \pm 0.1 \text{ GPa}$ for HTb (Fig. 1f; see Soret et al., 2017, for details). The preservation of prograde chemical zoning (over a $\text{dT} \geq 100^\circ\text{C}$ and a $\text{dP} \geq 0.1 \text{ GPa}$) suggests fast exhumation of the HT sole ($\leq 1\text{--}2 \text{ Ma}$) after reaching peak conditions at 95–96 Ma, as supported by radiometric dating (e.g., Hacker, 1990; Rioux et al., 2016).

5 The underlying LT sole (Fig. 1c) is mainly composed of greenschist facies metacherts, with imbrications of amphibole-bearing metatuffs, and is not considered here. Estimated peak P–T conditions are more loosely constrained at $530 \pm 50^\circ\text{C}$ and $0.5 \pm 0.1 \text{ GPa}$ (Fig. 1f; Soret et al., 2017).

The entire metamorphic sole shows a strong planar fabric with evidence of both pure and simple shear deformation (Figs. 2a-c). In the LT sole, the lattice preferred orientation of quartz in the inter-bedded quartzite is consistent with shear senses 10 observed in the basal banded peridotite (Boudier et al., 1988; Gray et Gregory, 2000; Ambrose et al., 2018). Deformation is less conspicuous in the garnet–clinopyroxene-bearing HTa sole compared to the HTb and LT soles, in which larger lithological heterogeneities exist. HTa amphibolite is indeed homogeneous (Figs. 1c, 2a-b), fine-grained and composed of amphibole + garnet + clinopyroxene \pm plagioclase, while HTb amphibolite is coarser-grained and consists of amphibole + plagioclase \pm epidote with rare biotite and plagioclase-rich imbricated layers (Figs. 1c, 2c).

15 4 Methods and sampling strategy

A suite of samples was collected from the two sub-units of the HT sole from three localities where the HT sole is the most complete and best preserved (Khubakhib, Sumeini and Wadi Tayin; Fig. 1b). Six samples (five from HTa and one from HTb; Fig. 1c, Table 1) were analysed using electron back-scattered diffraction (EBSD). For clarity, only microstructures of the most complete and representative section (the three HTa unit samples from Sumeini; see Soret et al., 2017) are detailed here.

20 Microstructural descriptions for the Khubakhib and Wadi Tayin sections are given as supplementary information.

EBSD data were collected using a CamScan X500FE CrystalProbe scanning electron microscope (SEM) at Géosciences Montpellier (France). Measurements were performed on polished thin sections at a 25 mm working distance with an accelerating voltage of 15 kV. For each sample (see map step size in Table 1), amphibole, plagioclase, clinopyroxene, garnet (together with prehnite, epidote and Ti-rich phases such as rutile, titanite and ilmenite) were indexed wherever present.

25 Resulting maps were first filtered using the Channel 5 software suite (Schmidt and Olesen, 1989) to increase the quality of the maps. Isolated pixels were removed, and non-indexed pixels with a minimum of 6 identical neighbours were filled with the same orientation. Maps were then processed using MTEX, a MATLAB toolbox for textural analysis (Hielscher and Schaeben, 2008; Bachmann et al., 2010; Mainprice et al., 2014).

In MTEX, misorientation angles (defined as the lowest rotation angle between two pixels about a common axis that brings two lattices into parallelism; e.g., Lloyd et al., 1997; Wheeler et al., 2001) were used to identify grain boundaries, applying a 10° threshold between adjacent pixels. Grains with a surface smaller than 10 pixels were discarded. Twins in plagioclase were distinguished from grain boundaries by filtering out the 178° to 180° misorientations during grain boundary identification. The 5 grain size for each mineral was calculated using the equivalent circle diameter. Pole figures were calculated using the crystallographic orientation of each grain (i.e., one point per grain). All plots are represented in lower hemisphere projections in the specimen reference frame, with contours as multiples of a uniform distribution. Since thin sections were not perfectly cut parallelly to the lineation (hardly visible on the hand specimen), the latter was defined on the pole figures by the amphibole c-axis maxima (point “X” in figures 8, 11 and 12). Mineral crystallographic preferred orientation (CPO) strength was 10 characterized using the J index (from 1 in the case of random orientation distribution to infinity in the case of an ideal single crystal; Bunge, 1982), calculated from the orientation distribution function (ODF; Mainprice et al., 2014). The shape preferred orientation (SPO) was calculated from the average orientation of the long axis of the best-fit ellipse of each grain. The aspect ratio (AR) of grains corresponds to the length ratio between the long and short axes of the best-fit ellipse. Kernel Average Misorientation (KAM) analysis was used to map intragranular misorientations in clinopyroxene, plagioclase and amphibole. 15 The KAM is defined as the average misorientation around a measurement point with respect to the 16 nearest neighbour points in a particular grain.

To track nucleation and dissolution-precipitation processes during the deformation of amphibole and clinopyroxene, composition maps (Figs. 6,7) were acquired with 1–3 µm spatial resolution. Major elements were measured at CAMPARIS (Sorbonne Univ.) using a CAMECA SX-5 electron microprobe. Classical analytical conditions were used (200 kV, 40 nA, 20 wavelength-dispersive spectroscopy mode), using Fe₂O₃ (Fe), MnTiO₃ (Mn, Ti), diopside (Mg, Si), orthoclase (Al, K), anorthite (Ca) and albite (Na) as standards. See Soret et al. (2017) for representative point analyses of garnet, amphibole, clinopyroxene, feldspar and epidote in these samples.

Mineral abbreviations used throughout the text and figures are given after Whitney and Evans (2010).

5 Results

25 5.1 Sample overview

Samples from the Sumeini HTa unit are presented structurally from top to bottom, starting from the highest-grade samples collected near the contact with the overlying peridotite to garnet-free samples away from the contact. Mineral occurrences and proportions are given in Table 1.

Within 2.5 m from the peridotite, the metamorphic sole is composed of a garnet-clinopyroxene bearing amphibolite. Peak 30 metamorphic assemblage and microstructures are well preserved in sample SE13-67 (Fig. 2d; Soret et al., 2017). The garnet-

clinopyroxene amphibolite SE13-67 exhibits a mylonitic foliation, locally transected at a relatively low angle (15–25°) by C'-type shear bands indicating a dextral shear sense in the thin-section frame. The foliation comprises fine-grained aggregates of brown amphibole and clinopyroxene, and locally garnet and clinopyroxene porphyroclasts (Fig. 2d). Three disjunctive domains are distinguished in thin-section:

5 – Area 1 (A1) is dominantly composed of a clinopyroxene aggregate aligned in the foliation, and is cut across at low angle by veins of epidote \pm prehnite \pm apatite (Figs. 2d, 3a).

– Area 2 (A2a, b) is composed of amphibole (50–65%) and clinopyroxene (25–35%) (Figs. 2d, 3b,c).

– Area 3 (A3) is composed of amphibole (42%), clinopyroxene (22%) and garnet (12%) (Figs. 2d, 3d).

10 Plagioclase is either rare or absent in the matrix, and most crystals have not been successfully indexed due to pervasive late sericitization by a minute assemblage of albite + epidote + muscovite. Epidote (≤ 2 vol.-%), apatite (≤ 1 vol.-%) and prehnite (≤ 5 %), commonly found in veins sub-parallel to the foliation (Fig. 2d), testify to a late stage of Ca-rich fluid circulation at low-T conditions ($\leq 700^\circ\text{C}$), which is documented across the entire HT metamorphic sole (Fig. 2b; Soret et al., 2017).

15 The degree of high-T (700 – 800°C) retrogression increases steadily towards the base of the HTa unit, and is maximum at the contact with the HTb unit (Soret et al., 2017). Rocks located further away from the sole-peridotite contact therefore mostly

15 record lower temperature associated with post-T-peak deformation. About 8 m beneath the peridotite (sample SE13-69; Fig. 4a), the metamorphic sole exhibits a coarser-grained, more conspicuous foliation characterized by higher proportions of brown amphibole (58%) and plagioclase (14%), partly replacing clinopyroxene (12%) and garnet (3%). About 25 m below the contact (sample SE13-76; Fig. 4b), garnet and clinopyroxene no longer coexist in the metamorphic sole. Amphibole (23%) has a brown to greenish-brown colour and is closely associated with plagioclase (64%), both with coarser grain size. Amphibole grains are 20 more scattered in the plagioclase-rich matrix and do not commonly form aggregates. The amphibolite also evidences precipitation of yellowish epidote (12%) aligned along C'-type shear bands together with fine-grained amphibole (Fig. 4b).

25 The underlying HTb unit is made of coarse-grained (typically 1 mm in diameter) plagioclase and greenish-brown amphibole aggregates, roughly in equal proportions, with rare, ≤ 50 cm-thick intercalations of biotite-plagioclase-rich amphibolite (Soret et al., 2017). Plagioclase-rich and darker amphibole-rich layers alternate throughout this unit (Fig. 2c).

25 **5.2 Microstructures**

5.2.1 Amphibole

The amphibole median grain size decreases towards the contact with the peridotite (Table 1; Figs. 3a-c), i.e. where peak-metamorphic textures are best-preserved (≤ 2.5 m; SE13-67). In this sample, the median grain size for amphibole associated with clinopyroxene (A2; 56–57 μm) is similar to that for amphibole associated with clinopyroxene and garnet (A3; 55 μm ;

30 Figs. 5a,b; Table 1). Most amphibole grains have a subhedral shape. Away from the peridotite, the amphibole median grain

size increases with increasing retrogression from 93 μm (at 8 m; SE13-69; Fig. 5c) to 110 μm (at 25 m; SE13-76; Fig. 5d), and the shape becomes more anhedral, commonly characterized by interstitial overgrowths at triple junctions with plagioclase (Fig. 5d).

Large amphibole grains display irregular boundaries in all samples, especially where bounded by -altered- plagioclase or 5 prehnite (Figs. 5c,d, 6a-d). They also show intragranular micro-fractures which are parallel to cleavage planes or perpendicular to the [001] direction (Fig. 6a-d). These micro-fractures locally dissect the large grains, forming smaller grains with straight and sharp intra-phase boundaries (Fig. 6a-d). Later and wider prehnite-filled fractures are also found transecting the amphibolite (Fig. 5b).

10 The mean aspect ratio of amphibole (1.9 ± 0.6) does not vary with the distance from the peridotite nor with the mineral assemblage (Fig. S2a). Amphibole shape-preferred orientation (SPO), subparallel to the shear plane, is very strong in all samples and its intensity correlates positively with grain size and aspect ratio (Fig. S2a).

In the HTa unit, only rare (<5%) amphibole grains show microstructural evidence for intra-crystalline plasticity, as undulatory or patchy extinction (Fig. 6a-b) and subgrain boundaries. However, in the sample best-preserved from retrogression (SE13- 15 67) the Kernel Average Misorientation (KAM) maps outline the presence of intracrystalline misorientations in most amphibole grains. Most of these misorientations are associated with significant rotations (up to 6° ; Fig. 6e-i). Grains with the high micro- fracture density show the highest misorientation angles or new grain boundaries (red arrows; Fig. 6a,e). In the more retrogressed samples (SE13-69, SE13-76), amphibole grains also show a high density of micro-fractures (Fig. 6c,d) which are associated with high intragranular misorientations (Fig. 6h,i). In both samples, some of these intracrystalline misorientations are spatially correlated with undulatory extinction and subgrain formation (Fig. 6c,h), especially in the largest and/or most 20 elongated amphibole grains (i.e., which can locally show intragranular fractures; Fig. 6d-i).

5.2.2 Garnet

Garnet grains have rounded to ellipsoidal shapes (Figs. 2d, 5a,b) and essentially form σ -type porphyroclasts showing a dextral sense of shear in the thin-section frame (Figs. 2d, 5a). Pressure shadows are composed of fine-grained amphibole and clinopyroxene. Garnet crystals are fractured and, locally, fragmented (Fig. 5b). These fractures cut across their prograde 25 growth zonation (Soret et al., 2017) and are filled with oriented, fine-grained mixtures of amphibole + clinopyroxene \pm rare plagioclase (Fig. 5b). Where retrogression is more pervasive (SE13-69), garnet is rimmed by plagioclase (Figs. 4a, 5c) and lacks of pressure shadows.

5.2.3 Clinopyroxene

Clinopyroxene grains have euhedral to ellipsoidal shapes (Figs. 2d, 5e-h). The aspect ratio of clinopyroxene is smaller than 30 that of amphibole (1.6 ± 0.4 on average) and does not vary with grain size, mineral assemblage or with the distance of the

samples to the peridotite contact (Fig. S2e). Within mono-mineralic layers (A1 in SE13-67; Figs. 2d, 3a, 5e), clinopyroxene has a median grain size of 31 μm (Fig. S2d). Where associated with amphibole (A2) and/or garnet (A3), the median grain size (51–57 μm) is similar to that of amphibole (Fig. S2d). Yet, clinopyroxene forms in places σ -type porphyroclasts (A2 in SE13-67; Figs. 2d, 3b-c, 5f) with high aspect ratios (≥ 2). They are usually aligned in the foliation plane (Figs. 2d, 5f, S2f) while the 5 SPO for small clinopyroxene grains are more random (Fig. S2f).

The core of clinopyroxene porphyroclasts is characterized by undulose extinction and trails of secondary fluid inclusions representing healed fluid-filled micro-fractures (dashed white arrows; Fig. 5g,h). Minute amphibole is found along the cleavages and the micro-fractures (white arrows; Fig. 5h). These trails are locally cut across by the wider prehnite-filled fractures.

10 Clinopyroxene mantle also shows elongated fine-grained wings (consistent with dextral sense of shear in the thin-section frame; Fig. 2d) composed of small grains of variable size but with a median value similar to that of the new grains scattered in the matrix and in monomineralic layers (A1). Some of these small grains display undulose extinction (Fig. 5h). However, they rarely contain micro-fractures. Interstitial small amphibole grains (green arrows; Fig. 5g-h), randomly oriented, are typically found in the porphyroblast mantle and wings at the triple junction of the new clinopyroxene grains (Figs. 5g-h).

15 Where garnet is present (A3 in SE13-67, SE13-69; Figs. 2d, 5a), clinopyroxene grains form fine-grained aggregates embedded in an amphibole-rich matrix. In sample SE13-67, most amphibole grains have a subhedral shape (Fig. 5a). However, the degree of phase mixing with amphibole in the matrix is higher than in Area 2, especially in sample SE13-69 characterized by precipitation of secondary amphibole at the expense of clinopyroxene.

5.2.4 Plagioclase

20 Plagioclase is rare, even in the best-preserved metamorphic sole samples. The analysis of the crystallographic orientation in plagioclase grains is complicated by retrogression, therefore the results shown below are restricted to the best-preserved grains, and may not be representative of all grains formed at high P-T.

5.3 Mineral composition mapping

5.3.1 Amphibole

25 Amphibole composition plots within the pargasite to actinolite fields (see Soret et al. (2017) for detailed analyses). Hereafter, amphibole is referred to as Ti-high (≥ 0.2 a.p.f.u.), Ti-medium (0.1–0.2 a.p.f.u.) and Ti-low (≤ 0.1 a.p.f.u.) amphibole.

In sample SE13-67, amphibole grains show an homogeneous Ti-high composition (Fig. 6j-k), confirming that these grains formed at or near peak conditions. Interstitial amphibole grains have a Ti-medium composition, indicating a nucleation during

the onset of cooling. The opaque mineral and veins found along amphibole grain boundaries and microfractures correspond to ilmenite (green arrow; Fig. 6a,b,j,k) which also formed at slightly lower P–T conditions (Soret et al., 2017).

In the samples marked by a higher degree of retrogression at amphibolite-facies conditions (SE13-69, SE13-76), amphibole grains evidence a much more complex and patchy zoning pattern including smaller Ti-rich areas than in sample SE13-67.

5 These Ti-rich areas are usually truncated by Ti-medium to Ti-low areas, especially along micro-fractures (red arrows; Figs. 6l-m). In addition to the precipitation of secondary plagioclase and ilmenite at amphibole lobate grain boundaries and/or along the micro-fractures (Fig. 6a-c), these zoning patterns indicate dissolution-precipitation during cooling (i.e., 800–700°C). This also further supports the observation that Ti-medium and Ti-low amphibole grains are not in equilibrium with clinopyroxene and garnet but rather with plagioclase.

10 5.3.2 Clinopyroxene

Clinopyroxene has a diopside-rich composition with small variations in jadeite content (Na, Al). Hereafter, clinopyroxene is distinguished as jadeite-rich ($Al > 0.2$ a.p.f.u) and jadeite-poor ($Al < 0.2$ a.p.f.u) clinopyroxene, recording the peak-pressure condition and the early exhumation conditions, respectively (Soret et al., 2017).

15 Clinopyroxene porphyroclasts have a jadeite-rich core similar in composition to that of inclusions in garnet, and a thin jadeite-poor rim (Fig.6a-c). The jadeite-rich core is truncated by micro-fractures which are both filled by Ti-rich to Ti-medium amphibole (red arrows; Fig.6a-c). At the edges of the largest microfractures dissecting the porphyroblast core, compositions are jadeite-poor.

20 Small clinopyroxene grains in mono- and poly-mineralic layers display a zoning pattern similar to that of the clinopyroxene porphyroclasts, with jadeite-rich cores rimmed and locally truncated by jadeite-poor domains (Fig.6a-c). As for clinopyroxene porphyroclasts, some of the small grains exhibit amphibole-bearing micro-fractures in the jadeite-rich core only.

5.4 Crystallographic preferred orientation

5.4.1 Amphibole

25 In all samples (SE13-67, SE13-69 and SE13-76), amphibole has a very strong CPO, with [001] axes (i.e., shortest Burgers vector; Hacker and Christie, 1990) mostly parallel to the lineation (Figs. 8a, 9a-c). Poles to (100) are subperpendicular to the foliation and poles to (010) are in the foliation, subperpendicular to the lineation (Fig. 8a). Poles to (100) always show the highest density and poles to (010) usually display the weakest preferred orientation.

Amphibole J-index ranges from 2.86 in the sample SE13-76 to 5.27 in the sample SE13-67 (Fig. 10a-b). The CPO strength is 30 slightly positively correlated with the modal proportion of amphibole but no systematic correlation is found with the distance

to the peridotite (Fig. 10a-b). In sample SE13-67, the CPO strength is significantly weakened around garnet and clinopyroxene porphyroclasts which show strong foliation deflection. In the more retrogressed sample SE13-69, where garnet and clinopyroxene coexist but do not deflect the foliation plane, amphibole has a strong CPO fabric (J-index = 3.67; Fig. 10a-b) as in the garnet-free layers of SE13-67 (Area 2a). The weakest CPO (J-index=2.87; Fig. 10a-b) is observed away from the contact 5 in the garnet-free sample SE13-76 which has the smallest amphibole modal proportion. Moreover, as highlighted with the SPO, amphibole grains with smaller grain size (< 80 μm) and/or aspect ratio (< 1.5) display a similar CPO pattern but significantly weaker in intensity compared to larger or more elongate grains (Fig. 10c).

The misorientation angle distribution of amphibole in all samples highly differs from the theoretical random distribution (i.e., the “uniform” green curve; Fig. 8b). This is consistent with the strong intensity of amphibole CPO. Small misorientation angles 10 (from 2 to 10°) are largely dominant. They correspond to rotations around the [001] axis, and to a much lesser extent around the [010] axis (Fig. 8c). The [010] axis concentration is slightly higher in sample SE13-76 compared to the other samples.

5.4.2 Clinopyroxene

Clinopyroxene has a moderate to weak CPO. As in amphibole, the [001] maximum is subparallel to the lineation but more dispersed (Fig. 9d-f, 11a, S5b). The majority of CPO patterns has girdle concentrations of both (100) and (010) poles, except 15 in sample SE13-69 where poles to (010) have a maximum normal to the foliation (Fig. 11a). In SE13-67, the strongest CPO (or J-index) is found within monomineralic layers of SE13-67 (J-index=2.61 in A1; Figs. 10a). In poly-mineralic aggregates, clinopyroxene J-index ranges from 1.21 to 1.73 (Fig. 10b). In contrast with amphibole, both the SPO and CPO strength of clinopyroxene appear to be also largely insensitive to grain size and aspect ratio (Fig. 10c).

The misorientation angle distribution of clinopyroxene in all samples does not significantly differ from the theoretical random 20 distribution (i.e., the “uniform” green curve; Fig. 11b), except in the monomineralic layer A1 in sample SE13-67. Small misorientation angles (from 2 to 10°) largely prevail. They correspond to rotations essentially around the [010] and the [001] axis (Fig. 11c), which corresponds to the mechanical twinning axis, as previously reported for clinopyroxene deformed at high temperature conditions (Frets et al., 2012).

5.4.3 Plagioclase

25 Plagioclase has a weak CPO (Fig. 12a, S5c-d). Its strength is similar to that of clinopyroxene, with a J-index varying between 1.51 and 2.06 (Fig. 10a). Plagioclase grains display a concentration of (001) poles normal to the foliation plane and [100] axes subparallel to the lineation (Fig. 12a). Poles to (010) show no preferred alignment. The CPO strength and patterns do not vary with the distance from the contact, nor with the mineral assemblage.

The misorientation angle distribution of plagioclase in all samples slightly differs from the theoretical random distribution 30 (i.e., the “uniform” green curve; Fig. 12b). Small misorientation angles (from 2 to 10°) are largely dominant. They correspond

to rotations around the twinning axis [100], and to a much lesser extent around the [001] axis (Fig. 12c). However, the [001] axis becomes the main axis of intracrystalline misorientations in sample (SE13-76), where plagioclase forms monomineralic aggregates (Fig. 12a).

6 Discussion

5 The HTa metamorphic sole unit is characterized by an intense gradient of syn-kinematic retrogression increasing toward its base. This gradient allows us to constrain the combined deformation mechanisms in amphibolites at peak conditions (~850°C – 1GPa; in sample SE13-67) and during cooler and more hydrated conditions (~800 and ~750°C and 0.7 GPa, in samples SE13-69 and SE13-76, respectively).

10 Amphibolites recording peak conditions (e.g. SE13-67) show large contrasts in mineral strength and crystallographic fabric. Clinopyroxene forms σ -type porphyroclasts and monomineralic fine-grained aggregates wrapped around by monomineralic aggregates of amphibole or polymimetic aggregates of amphibole + clinopyroxene \pm plagioclase (Fig. 2d). Where garnet is present, clinopyroxene forms fine-grained aggregates partially mixed within an amphibole-rich matrix. Clinopyroxene appears therefore to be mechanically stronger than amphibole and the polymimetic matrix, but weaker than garnet. Yet, such a strength contrast disappears in the more retrogressed garnet-clinopyroxene amphibolite (SE13-69) where mineral reactions are more pervasive.

Moreover, clinopyroxene aggregates show ubiquitous plastic deformation (as indicated by the presence of undulose extinction; Fig. 5g-h) but display a weak CPO. By contrast, amphibole aggregates in the amphibolites of the HT metamorphic sole have

20 a very strong CPO (J -index ~ 5 ; Fig. 10) despite showing no or only little evidence for intracrystalline plastic deformation. Extensive phase mixing is observed throughout the rock, especially in more retrogressed samples. Finally, amphibole, clinopyroxene and garnet underwent intense grain size reduction by micro-fracturing, closely associated with fluid-driven mineral reactions.

25 In the light of our observations (see also Table 2) we discuss below the possible deformation mechanisms and their relative contributions to the mechanical behaviour of the amphibolites of the soles.

6.1 Deformation processes in amphibolite

6.1.1 Dislocation creep

Amphibole SPO and CPO are similar in orientation to what is commonly reported for strained amphibole (Berger and Stünitz, 1996; Cao et al., 2010; Díaz Aspiroz et al., 2007; Elyaszadeh et al., 2018; Getsinger et al., 2013; Gomez Barreiro et al., 2010; Hacker and Christie, 1990; Imon et al., 2004; Tatham et al., 2008). They are also consistent with the extreme tectonic thinning

and large shear strain of the HT metamorphic soles ($\gamma \geq 5$; Soret et al., 2017). For amphibole with J-index of ~3 and ~5, shear strains of ≥ 5 and ≥ 10 have been reported in amphibolite in deformation experiments (Getsinger, 2015) and in continental shear zones (Tatham et al., 2008), respectively (Fig. 10a). As for amphibole in the Semail HT metamorphic sole, those amphibole crystals show no or little evidence for intracrystalline plastic deformation and coexisting phases (plagioclase, 5 clinopyroxene and quartz) have a weak CPO.

If the strong amphibole CPO and the apparent intracrystalline misorientations (Fig. 8) result from plastic deformation, the misorientation axis should be perpendicular to the direction of crystal slip (e.g., Lloyd et al., 1997). In our study, however, intracrystalline misorientations are essentially accommodated around the [001] axis, and only to a lesser extent around the [010] axis (Fig. 8b). Most of the misorientations are therefore incompatible with the activation of the amphibole easy slip 10 system (100)[001] that would account for the observed CPO geometries and intracrystalline misorientations (Fig. 8a). Conversely, the [010] rotation axis (Fig. 8b), lying in the foliation plane perpendicularly to the general shear sense, is compatible with the activation of the amphibole easy slip system. The relatively small number of rotation axes oriented parallel to [010] is also consistent with the fact that only few of the Ti-rich amphibole grains recording peak T conditions (~850°C) show microstructural evidence for plastic deformation (such as subgrain formation; SE13-67; Fig. 9a-c).

15 Clinopyroxene has a CPO pattern characterized by the [001] axis maximum subparallel to the lineation (Figs. 9d-f, 11a), and girdle concentrations of both (100) and (010) poles perpendicular to the lineation (Figs. 11a). This pattern reflects the dominant activation of the $\{hk0\}[001]$ glide systems in the dislocation creep regime, as commonly reported in experiments on omphacite and diopside (Bascou et al., 2002; Getsinger and Hirth, 2014; Ingrin et al., 1991). This is consistent with the intracrystalline misorientations accommodated around the [010] axis (Fig. 11c), especially dominant in the fine-grained monomineralic 20 aggregates. However, the CPO strength is low to moderate with some dispersion of the [001] axis even in the fine-grained monomineralic aggregates (Figs. 11a, S5b).

6.1.2 Brittle deformation

The high micro-fracture densities in coarse amphibole grains (Figs. 5a, 6a-b) and the general fine-grained size in the best 25 preserved sample (SE13-67) attest to grain size reduction through extensive brittle deformation starting at or after peak conditions. Healed micro-fracturing in secondary amphibole crystals grown during retrograde P-T conditions (in SE13-69 and SE13-76) indicates that brittle deformation also persisted during cooling. This is further supported by the ubiquitous presence of wider epidote- and prehnite-filled fractures crosscutting the entire HT amphibolite (Fig. 2d).

The brittle behaviour of amphibole within a rock deforming ductilely at high temperature has already been reported (Nyman et al., 1992; Berger and Stunitz, 1996; Imon et al., 2002; Diaz Aspiroz et al., 2007; Gomez Barreiro et al., 2010; Ko and Jung, 30 2015; Marti et al., 2017; Giuntoli et al., 2018) but ascribed to significantly lower deformation temperatures ($\leq 700^{\circ}\text{C}$). Preferential micro-fracturing along planes including the long ([001]) crystallographic axis could explain the similar aspect

ratios of fine and coarse amphibole grains (essentially ≤ 2 –3, as suggested by Gomez Barreiro et al. (2010). Micro-fracturing along the [001] crystallographic axis together with small rigid rotations (1–3°; Fig. 6e–h) may further explain some of the apparent intracrystalline misorientations in amphibole around the [001] rotation axis (Figs. 6j, 8c)

Intense grain size reduction through brittle deformation in fact affected the whole rock at or near peak conditions as attested by the presence of fractured and rotated garnet and jadeite-rich clinopyroxene porphyroclasts in sample SE13-67. The lack of micro-fractures in the new small clinopyroxene suggests that fracturing preferentially occurred along cleavage planes of the porphyroclasts, and the precipitation of minute amphibole along these cleavage planes has probably facilitated the failure. Moreover, the intense brittle deformation followed by small rigid rotation easily explained the general weak of the CPO of clinopyroxene in the amphibolite.

The strong correlation between the aspect ratio, the CPO and SPO intensities of primary and secondary amphibole in all samples (Fig. 10) also advocates for a component of rigid grain rotation in the strain accommodation from peak to retrograde conditions (as previously reported in other settings; Ildefonse et al. 1990; Shelley 1994; Berger and Stünitz 1996; Díaz Azpiroz et al. 2007; Tatham et al. 2008; Elyaszadeh et al., 2018). Contrary to clinopyroxene, the high aspect ratio of amphibole allowed the preferential alignment of the long axes parallel to the stretching direction. Yet, the strong SPO/CPO parallel to the lineation in secondary amphibole could also be explained by oriented dissolution-precipitation during cooling conditions (e.g.,; Shelley, 1994; Berger and Stünitz, 1996).

6.1.3 Dissolution-precipitation creep and grain boundary sliding

Lobate boundaries and patchy zoning of amphibole defined by Ti-high cores truncated by the precipitation of Ti-medium/low areas reveal that brittle deformation was closely associated with and/or promoted dissolution precipitation (Fig. 6k–m). This is also indicated by the nucleation of Ti-medium amphibole and jadeite-poor clinopyroxene within micro-fractures and cleavages of diopside-rich clinopyroxene (Figs. 5g, 7).

Dissolution-precipitation creep was likely driven by the metastability of the peak assemblage during cooling and hydration, and was further enhanced by the permeability created by the micro-fracturing. Such a positive feedback between viscous and/or brittle deformation and (hydrous) mineral reactions was recently described in shear experiments on amphibolites conducted at 600–800°C and 0.5–1.5 GPa (Marti et al., 2017, 2018). The tight relationship between brittle deformation and dissolution-precipitation creep advocates for transient changes in pore-fluid pressure, either during dehydration (and/or melting) at peak conditions (e.g., Brodie and Rutter, 1985) or during the onset of retrogression (i.e., fluid ingress from adjacent slab dehydration; e.g., in a colder subduction context: Locatelli et al., 2018).

The presence of randomly-oriented minute amphibole at the grain boundaries of mantled clinopyroxene and the general intense phase mixing in the poly-mineralic matrix testify to the activation of grain boundary sliding (GBS) as a dominant mechanism

accompanying dissolution precipitation creep syn to post grain size reduction, even in the mono-mineralic layers (A1; SE13-67). The absence, in the retrogressed HTa amphibolite (sample SE13-69; Fig. 3a) of microstructural evidence (e.g. pressure shadows) for any strength contrast between phases known to have different strength further supports the role of GBS.

6.3 Mechanical evolution of the plate interface during subduction infancy

5 During initial subduction progress, the leading edge of the slab encounters an increasingly warmer, anhydrous mantle wedge acting as a buttress (Fig. 14a; Agard et al., 2016). Accretion of metamorphic soles to the basal peridotites of the future ophiolite reflects this increased mechanical coupling between the plates across a restricted P–T-time window (i.e., when viscosities of the slab crust and overlying mantle are similar; Agard et al., 2016). Our micro-structural data allow to document the evolution of the deformation at the top of the slab (stages A1-A2-B; Figs. 13, 14):

10 — Approximatively from amphibolite to granulite facies and up to $850 \pm 50^\circ\text{C}$ – 1.0 GPa, the slab crust progressively dehydrates and minerals such as amphibole (Ti-medium/poor) and plagioclase are replaced by mechanically stronger garnet and clinopyroxene in the HTa unit (and Ti-rich amphibole; stage A1; Fig. 13a). The leading edge of the slab thus likely hardens (as shown by the evolution of the strength curve in figure 14). When it reaches the strength of the mantle on top, HTa gets stripped and becomes the first slice accreted to the upper plate peridotite (stage A; Fig. 14). Our observations indicate that a

15 strong amphibole fabric dominates rock anisotropy at the top of the slab. This fabric is controlled by syn-kinematic oriented growth and rigid grain rotation, as shown by the strong correlation between grain size, aspect ratio and fabric intensity. The onset of brittle deformation in the garnet–clinopyroxene amphibolite leads to drastic grain size reduction (GSR; stage A1; Fig. 13a). This brittle deformation, possibly controlled by dehydration embrittlement (Davies, 1999), dehydration-driven stress transfer (Ferrand et al., 2017) and/or fluid ingressoin from adjacent slab dehydration acts as a precursor for strain localization

20 in the garnet–clinopyroxene amphibolite within the downgoing slab (and therefore detachment of HTa; Fig. 14). Similarly, fluids released at the plate interface during slab burial are thought to trigger early strain softening of the base of the mantle wedge through GSR promoted by fluid/mantle interaction and dissolution/precipitation processes (Fig. 14b; Prigent et al. 2018b; Soret et al., 2016). Overall, these combined processes controlled the onset and location of strong mechanical coupling across the plate interface, between the top of the slab and the base of the nascent mantle wedge (stage A; Fig. 14).

25 — from 850 down to 750°C and 1 to 0.7 GPa (stage A2 in Fig. 13a), early exhumation and cooling of the garnet–clinopyroxene bearing HTa is associated with strong shearing and pervasive retrogression across the plate interface (Soret et al., 2017; Prigent et al., 2018b). Deformation in HTa is extensively accommodated by dissolution-precipitation assisted by grain boundary sliding (including mineral reactions, heterogeneous nucleation and phase mixing), leading to a second stage of significant strain softening of the exhuming HTa unit. Dissolution-precipitation creep and GBS are closely related to the brittle

30 deformation events observed from peak conditions and operating until late exhumation (see sect. 6.3) which facilitate fluid ingressoin and thereby enhanced mineral reactions and rock re-equilibration within HTa. Syn-exhumation mechanical

softening occurs also in the basal mantle wedge in the diffusion creep regime, as it becomes colder and more metasomatized (Fig. 14; Agard et al., 2016; Prigent et al., 2018a,b; Soret et al., 2016). Similar weakening on both sides of the plate interface maintains a coupling between HTa and the peridotites and explains their coeval early exhumation (from ~ 1 to 0.7 GPa).

— At temperatures around 750°C (stage B: Fig. 12b; Fig. 14), during later exhumation and cooling of HTa, pervasive fluid-rock interaction transforms the base of HTa into a two-phase matrix composed of syn-kinematic Ti-medium/low amphibole and plagioclase, with only minor amount of biotite and epidote. Meanwhile, the top of the subducting slab (i.e., the future plagioclase-rich HTb unit) consists of a similar mineral assemblage (Fig. 14). Our observations show that GBS is progressively inhibited while dissolution–precipitation creep remains the dominant deformation mechanism, thus behaving potentially like the HTb unit. In the absence of significant GBS, the modal increase in (wet) plagioclase has a major softening effect.

10 Mechanical coupling between HTb and HTa and/or HTb and the weakening at the base of the mantle wedge is responsible for the detachment and accretion of HTb (Fig. 14).

These deformation stages between 850 and 750°C result in the extreme thinning and distribution of similar HT metamorphic soles below the ophiolite (shear strain ≥ 5) and in the thinning of the base of the ophiolite itself (see discussion in Casey and Dewey, 2013).

15 6.4 Mechanical implications for warm subduction zones and oceanic/continental crustal-scale shear zones

We envision at least three major implications of this record of progressive deformation in metamorphic soles:

— Since pressure is not expected to significantly influence deformation mechanisms in the ductile regime, we argue that deep recoupling mechanisms in mature warm subduction zones (at $T \geq 800^\circ\text{C}$; e.g., Nankai, Cascadia; Wada and Wang, 2009; Abers et al., 2017) could be controlled, as for HTa metamorphic soles, by the extent of fluid-rock interactions and the degree of 20 stability of high-pressure amphibole.

— Dissolution-precipitation creep and associated amphibole-forming reactions coupled with brittle deformation may also control strain localization at high temperature conditions, and therefore the development of long-lived oceanic detachments and core complexes in slow-spreading environments (Boschi et al., 2006; Escartin et al., 2003; Gölcher et al., 2019), as well 25 as continental crustal-scale shear zones in collisional settings under cooling conditions and exhumation (Getsinger et al., 2013; Giuntoli et al., 2018; Tatham et al., 2008).

— Finally, while many different interpretations have been invoked for the deformation mechanisms of amphibole and amphibolites (e.g., GBS, diffusion creep, dislocation creep; see sect. 2), such diversity could reflect change in P-T conditions, water activity and mineral stability. This study outlines that ongoing metamorphic processes and amphibole stability should be carefully taken into account when interpreting deformation mechanisms in amphibole, especially in shear zones

experiencing hydration and cooling during exhumation, as a well-developed CPO in amphibole does not systematically testify to dislocation creep, and does not exclude a component of fracturing and GBS in sheared amphibolites.

7 Conclusions

Based on micro-structural analysis and mineral chemistry, this study highlights the mineral-scale mechanisms controlling the progressive deformation of sheared amphibolites from the Oman metamorphic sole during subduction infancy, and unravels how strain is localized and accommodated in (hydrated) mafic rocks under amphibolite and granulite facies conditions.

Metamorphic reactions and pore-fluid pressures driven by changes in P–T conditions and/or water activity exert a key control on the rheology of mafic rocks and the transition between brittle and viscous deformations at high temperature conditions (as noted experimentally; Marti et al., 2017, 2018).

At $850 \pm 50^\circ\text{C}$ and 1 GPa, garnet-clinopyroxene amphibolites accommodate large shear strain essentially through fracturing, grain size reduction and grain boundary sliding, confirming that amphibole and amphibolite has only little ability to deform in the dislocation creep regime. The exact driving mechanism for the fracturing remains uncertain. Possible explanations include dehydration embrittlement, dehydration-driven stress transfer and/or fluid ingression.

Lower temperatures ($800 - 700^\circ\text{C}$) and higher hydrated conditions on the return path lead to higher rock disequilibrium and therefore pervasive hydrous reactions. Strain in the exhumed amphibolite is dominantly accommodated in the dissolution-precipitation creep regime assisted and enhanced by a component of brittle deformation. Grain size reduction through fracturing and heterogeneous nucleation enables GBS and significant phase mixing, thereby producing a large mechanical weakening. However, the fabric intensity of amphibole is not significantly affected by the GBS activation (contrary to clinopyroxene and plagioclase) due to its specific high aspect ratio.

These mechanical evolutions, marked by strain hardening during increasing P–T conditions and dehydration and later, large strain softening during cooling and hydration, are respectively coeval with the detachment and early exhumation of the different amphibolitic units of the HT metamorphic sole. They likely control the extent of the viscosity contrast and, therefore, the mechanical coupling between the top of the slab and the peridotites across the plate interface during subduction infancy (Agard et al., 2016; Prigent et al., 2018b).

As amphibole is commonly found with plagioclase, clinopyroxene and/or garnet in high-temperature shear zones, these largely pressure-independent findings may be applied to other geodynamic environments where similar temperatures, lithologies, fluid circulation and mechanical coupling between mafic rocks and peridotites prevail, such as in mature warm subduction zones (e.g., Nankai, Cascadia), in lower continental crust shear zones and oceanic detachments

Author contributions

MS, PA and BD conceived the initial idea of the study. MS, PA, BD and CP participated in the fieldwork. MS conducted EBSD and EMP analyses. MS and BI performed EBSD data processing using MTEX. MS prepared the manuscript with contributions from all co-authors.

5 Competing interests

The authors declare no competing interests.

Acknowledgment

We thank F. Barou (Univ. Montpellier, France) for technical support on EBSD, N. Rividi and M. Fialin (CAMPARIS, Sorbonne Univ., Paris, France) for technical support on EMP, C. Nevado and D. Delmas (Univ. Montpellier) for the polishing 10 of thin-sections, and L. Labrousse, E. Gnos, P. Yamato and R. Graziani for helpful discussions. This work was essentially funded through the ONLAP project (ANR blanche, SIMI6; 2010 BLAN 615 01). Additional support was provided by an IUF grant (Institut universitaire de France) to PA.

References

Abers, G. A., Van Keken, P. E., and Hacker, B. R. The cold and relatively dry nature of mantle forearcs in subduction zones. 15 Nat. Geosci., 5, 333–337. doi:10.1038/ngeo2922. 2017.

Agard, P., Yamato, P., Soret, M., Prigent, C., Guillot, S., Plunder, A., Chauvet, A., and Monié, P. Plate interface rheological switches during subduction infancy: control on slab penetration and metamorphic sole formation. Earth Planet. Sc. Lett., 451, 208–220. doi:10.1016/j.epsl.2016.06.054. 2016.

Agard, P., Plunder, A., Angiboust, S., Bonnet, G., and Ruh, J. The subduction plate interface: Rock record and mechanical 20 coupling (from long to short time scales). Lithos. doi.org:10.1016/j.lithos.2018.09.029. 2018.

Ambrose, T. K., Wallis, D., Hansen, L. N., Waters, D. J., and Searle, M. P. Controls on the rheological properties of peridotite at a palaeosubduction interface: A transect across the base of the Oman–UAE ophiolite. Earth Planet. Sc. Lett., 491, 193–206. doi.org/10.1016/j.epsl.2018.03.027. 2018.

Bachmann, F., Hielscher, R., and Schaeben, H. Texture Analysis with MTEX – Free and Open Source Software Toolbox. Sol. 25 St. Phen., 160, 63–68. doi:10.4028/www.scientific.net/SSP.160.63. 2010.

Bascou, J., Tommasi, A., and Mainprice, D. Plastic deformation and development of clinopyroxene lattice preferred orientations in eclogites. J. Struct. Geology, 24, 1357–1368. doi:10.1016/S0191-8141(01)00137-7. 2002.

Berger, A., and Stünitz, H. Deformation mechanisms and reaction of hornblende: examples from the Bergell tonalite (Central Alps). *Tectonophysics*, 257, 149–174. doi:10.1016/0040-1951(95)00125-5. 1996.

Boschi, C., Früh-Green, G. L., Delacour, A., Karson, J. A., and Kelley, D. S. Mass transfer and fluid flow during detachment faulting and development of an oceanic core complex, Atlantis Massif (MAR 30°N). *Geochem. Geophys. Geosy.*, 7, Q01004. 5 doi:10.1029/2005GC001074. 2006.

Boudier, F., Ceuleneer, G., and Nicolas, A. Shear zones, thrusts and related magmatism in the Oman ophiolite: Initiation of thrusting on an oceanic ridge. *Tectonophysics*, 151, 275–296. doi:10.1016/0040-1951(88)90249-1. 1988.

Brodie, K. H. Variation in amphibole and plagioclase composition with deformation. *Tectonophysics*, 78, 385–402. doi:10.1016/0040-1951(81)90021-4. 1981.

10 Brodie, K. H., and Rutter, E. H. On the relationship between rock deformation and metamorphism with special reference to the behaviour of basic rocks. *Metamorphic Reactions*, 4, 138–179. doi:10.1007/978-1-4612-5066-1_6. 1985.

Bunge, H. J. *Texture Analysis in Materials Science*, Butterworth's, London, 351–401. 1982.

Bystricky, M., and Mackwell, S. Creep of dry clinopyroxene aggregates. *J. Geophys. Res.*, 106, 13443. doi:10.1029/2001JB000333. 2001.

15 Cao, S., Liu, J., and Leiss, B. Orientation-related deformation mechanisms of naturally deformed amphibole in amphibolite mylonites from the Diancang Shan, SW Yunnan, China. *J. Struct. Geology*, 32, 606–622. doi:10.1016/j.jsg.2010.03.012. 2010.

Davies, H. L. The role of hydraulic fractures and intermediate-depth earthquakes in generating subduction-zone magmatism. *Nature*, 328, 142–145. doi:10.1038/18202. 1999.

Dewey, J. F., and Casey, J. F. The sole of an ophiolite: the Ordovician Bay of Islands Complex, Newfoundland. *J. Geol. Soc. London*, 170, 715–722. doi:10.1144/jgs2013-017. 2013.

20 Díaz Aspiroz, M., Lloyd, G. E., and Fernández, C. Development of lattice preferred orientation in clinoamphiboles deformed under low-pressure metamorphic conditions. A SEM/EBSD study of metabasites from the Aracena metamorphic belt (SW Spain). *J. Struct. Geology*, 29, 629–645. doi:10.1016/j.jsg.2006.10.010. 2007

Dimanov, A., Rybacki, E., Wirth, R., and Dresen, G. Creep and strain-dependent microstructures of synthetic anorthite-diopside aggregates. *J. Struct. Geology*, 29, 1049–1069. doi:10.1016/j.jsg.2007.02.010. 2007.

25 Elyaszadeh, R., Prior, D. J., Sarkarinejad, K., and Mansouri, H. Different slip systems controlling crystallographic preferred orientation and intracrystalline deformation of amphibole in mylonites from the Neyriz mantle diapir, Iran. *J. Struct. Geology*, 107, 38–52. doi: 10.1016/j.jsg.2017.11.020. 2018

Ernst, W., and Liu, J. Experimental phase-equilibrium study of Al-and Ti-contents of calcic amphibole in MORB - A semiquantitative thermobarometer. *Am. Mineral.*, 83, 952–969. doi: 10.2138/am-1998-9-1004. 1998.

30 Escartín, J., Mével, C., MacLeod, C. J., and McCaig, A. M. Constraints on deformation conditions and the origin of oceanic detachments: The Mid-Atlantic Ridge core complex at 15°45' N. *Geochem. Geophys. Geosy.*, 4. doi:10.1029/2002GC000472. 2003.

Ferrand, T. P., Hilairet, N., Incel, S., Deldicque, D., Labrousse, L., Gasc, J., ... Schubnel, A. Dehydration-driven stress transfer triggers intermediate-depth earthquakes. *Nat. Commun.*, 8, 1–11. doi.org/10.1038/ncomms15247. 2017.

Getsinger, A. J. The Rheology of Amphibolite. Brown University. Ph.D. Thesis. 2015.

Getsinger, A. J., Hirth, G., Stünitz, H., and Goergen, E. T. Influence of water on rheology and strain localization in the lower 5 continental crust. *Geochem. Geophys. Geosy.*, 14, 2247–2264. doi:10.1002/ggge.20148. 2013.

Getsinger, A. J., and Hirth, G. Amphibole fabric formation during diffusion creep and the rheology of shear zones. *Geology*, 42, 535–538. doi:10.1130/G35327.1. 2014.

Giuntoli, F., Menegon, L., and Warren, C. J. Replacement reactions and deformation by dissolution and precipitation processes in amphibolites. *J. Metamorph. Geol.* doi.org/10.1111/jmg.12445. 2018.

10 Gnos, E. Peak Metamorphic Conditions of Garnet Amphibolites Beneath the Semail Ophiolite: Implications for an Inverted Pressure Gradient. *Int. Geol. Rev.*, 40, 281–304. doi:10.1080/00206819809465210. 1998.

Gómez Barreiro, J., Martínez Catalán, J. R., Prior, D., Wenk, H. -R., Vogel, S., Díaz García, F., Arenas, R., Sanchez Martinez, S., and Lonardelli, I. Fabric Development in a Middle Devonian Intraoceanic Subduction Regime: The Careón Ophiolite (Northwest Spain). *J. Geol.*, 118, 163–186. doi.org/10.1086/649816. 2010.

15 Gray, D. R., and Gregory, R. T. Implications of the structure of the Wadi Tayin metamorphic sole, the Ibra-Dasir block of the Samail ophiolite, and the Saih Hatah window for late stage extensional ophiolite emplacement, Oman. *Mar. Geophys. Res.*, 21, 211–227. doi:10.1023/A:1026772717865. 2000.

Guilmette, C., Smit, M. A., Hinsbergen, D. J. J. Van, Gürer, D., Corfu, F., Charette, B., ... Savard, D. Forced subduction initiation recorded in the sole and crust of the Semail Ophiolite of Oman. *Nat. Geosci.* doi:10.1038/s41561-018-0209-2. 2018.

20 Gölcher, A. J. P., Beaussier, S. J., and Gerya, T. V. On the formation of oceanic detachment faults and their influence on intra-oceanic subduction initiation: 3D thermomechanical modeling. *Earth Planet. Sc. Lett.*, 506, 195–208. doi:10.1016/j.epsl.2018.10.042. 2019.

Hacker, B. R. Simulation of the metamorphic and deformational history of the metamorphic sole of the Oman ophiolite. *J. Geophys. Res.-Solid Earth*, 95, 4895–4907. doi:10.1029/JB095iB04p04895. 1990.

25 Hacker, B. R., and Christie, J. M. Brittle/Ductile and Plastic/Cataclastic Transitions in Experimentally Deformed and Metamorphosed Amphibolite. *Geoph. Monog. Series.*, 56, 127–148. doi:10.1029/GM056p0127. 1990.

Hielscher, R., and Schaeben, H. A novel pole figure inversion method: Specification of the MTEX algorithm. *J. Appl. Crystallography*, 41, 1024–1037. doi:10.1107/S0021889808030112. 2008

Hier-Majumder, S., Mei, S., and Kohlstedt, D. L. Water weakening of clinopyroxenite in diffusion creep. *J. Geophys. Res.-Sol. Ea.*, 110, 1–12. doi:10.1029/2004JB003414. 2005.

Ildefonse, B., Lardeaux, J. M., and Caron, J. M. The behavior of shape preferred orientations in metamorphic rocks: amphiboles and jadeites from the Monte Mucrone area (Sesia-Lanzo zone, Italian Western Alps). *J. Struct. Geology*, 12, 1005–1011. doi:10.1016/0191-8141(90)90096-H. 1990.

Ildefonse, B., Sokoutis, D., and Mancktelow, N. S. Mechanical interactions between rigid particles in a deforming ductile matrix. Analogue experiments in simple shear flow. *J. Struct. Geology*, 14, 1253–1266. doi:10.1016/0191-8141(92)90074-7. 1992.

5 Imon, R., Okudaira, T., and Kanagawa, K. Development of shape- and lattice-preferred orientations of amphibole grains during initial cataclastic deformation and subsequent deformation by dissolution-precipitation creep in amphibolites from the Ryoke metamorphic belt, SW Japan. *J. Struct. Geology*, 26(5), 793–805. doi:10.1016/j.jsg.2003.09.004. 2004.

Ingrin, J., Doukhan, N., and Doukhan, J. C. High-Temperature Deformation of Diopside Single-Crystal .2. Transmission Electron-Microscopy Investigation Of The Defect Microstructures. *J. Geophy. Res.-Solid Earth And Planets*, 96, 14287–14297. doi:10.1029/91JB01233. 1991.

10 Ji, S., Shao, T., Michibayashi, K., Long, C., Wang, Q., Kondo, Y., Zhao, W., Wang, H., and Salisbury, M. H. A new calibration of seismic velocities, anisotropy, fabrics, and elastic moduli of amphibole-rich rocks. *J. Geophy. Res.-Sol. Ea.*, 118, 4699–4728. doi: 10.1002/jgrb.50352. 2013.

Kenkmann, T., and Dresen, G. Dislocation microstructure and phase distribution in a lower crustal shear zone - An example from the Ivrea-Zone, Italy. *Int. J. Earth Sci.*, 91, 445–458. doi:10.1007/s00531-001-0236-9. 2002.

15 Kim, D., Katayama, I., Wallis, S., Michibayashi, K., Miyake, A., Seto, Y., and Azuma, S. Deformation microstructures of glaucophane and lawsonite in experimentally deformed blueschists: Implications for intermediate-depth intraplate earthquakes. *J. Geophy. Res.-Sol. Ea.*, 120, 1229–1242. doi:10.1002/2014JB011528. 2015.

Ko, B., and Jung, H. Crystal preferred orientation of an amphibole experimentally deformed by simple shear. *Nat. Commun.*, 6, 6586. doi:10.1038/ncomms7586. 2015.

20 Kruse, R., and Stünitz, H. Deformation mechanisms and phase distribution in mafic high-temperature mylonites from the Jotun Nappe, southern Norway. *Tectonophysics*, 303, 223–249. 1999.

Locatelli, M., Verlaguet, A., Agard, P., Federico, L., and Angiboust, S. Intermediate-depth brecciation along the subduction plate interface (Monviso eclogite, W. Alps). *Lithos*, doi:10.1016/j.lithos.2018.09.028. 2018.

Lloyd, G. E., Farmer, A. B., and Mainprice, D. Misorientation analysis and the formation and orientation of subgrain and grain 25 boundaries. *Tectonophysics*, 279, 55–78. doi:10.1016/S0040-1951(97)00115-7. 1997.

Lloyd, G. E., Butler, R. W. H., Casey, M., Tatham, D. J., and Mainprice, D. Constraints on the seismic properties of the middle and lower continental crust. *Geol. Soc. Spec. Publ.*, 360, 7–32. doi:10.1144/SP360.2. 2011.

Mainprice, D., and Nicolas, A. Development of shape and lattice preferred orientations: application to the seismic anisotropy of the lower crust. *J. Struct. Geology*, 11, 175–189. doi:10.1016/0191-8141(89)90042-4. 1989.

30 Mainprice, D., Bachmann, F., Hielscher, R., Schaeben, H. Descriptive tools for the analysis of texture projects with large datasets using MTEX: strength, symmetry and components. *Geol. Soc. Spec. Publ.*, 409, 251–271. doi:10.1144/SP409.8. 2014.

Marti, S., Stünitz, H., Heilbronner, R., Plümper, O., and Drury, M. Experimental investigation of the brittle-viscous transition in mafic rocks – Interplay between fracturing, reaction, and viscous deformation. *J. Struct. Geology*, 105, 62–79. doi:10.1016/j.jsg.2017.10.011. 2017.

Nicolas, A., Boudier, F., Ildefonse, B., and Ball, E. Accretion of Oman and United Arab Emirates ophiolite – Discussion of a new structural map. *Mar. Geophy. Res.*, 21, 147–179. doi:10.1023/A:1026769727917. 2000.

Nyman, M. W., Law, R. D., and Smelik, E. A. Cataclastic deformation for the development of core mantle structures in amphibole. *Geology*, 20, 455–458. doi:10.1130/0091-7613(1992)020<0455. 1992.

5 Plunder, A., Agard, P., Chopin, C., Soret, M., Okay, A. I., and Whitechurch, H. Metamorphic sole formation, emplacement and blueschist facies overprint: early subduction dynamics witnessed by western Turkey ophiolites. *Terra Nova*, 28(5), 329–339. doi.org:10.1111/ter.12225. 2016.

Prigent, C., Guillot, S., Agard, P., Lemarchand, D., Soret, M., and Ulrich, M. Transfer of subduction fluids into the deforming mantle wedge during nascent subduction: Evidence from trace elements and boron isotopes (Semail ophiolite, Oman). *Earth 10 Planet. Sc. Lett.*, 484, 213–228. doi.org:10.1016/j.epsl.2017.12.008. 2018a.

Prigent, C., Guillot, S., Agard, P., and Ildefonse, B. Fluid-Assisted Deformation and Strain Localization in the Cooling Mantle Wedge of a Young Subduction Zone (Semail Ophiolite). *J. Geophy. Res.-Sol. Ea.*, 1–21. doi.org:10.1029/2018JB015492. 2018b.

Prigent, C., Agard, P., Guillot, S., Godard, M. and Dubacq, B. Mantle wedge deformation during subduction infancy: evidence 15 from the base of the Semail ophiolitic mantle, *J. Petrol.*, egypt090, doi:10.1093/petrology/egy090. 2018c.

Rioux, M., Garber, J., Bauer, A., Bowring, S., Searle, M., Kelemen, P., and Hacker, B. Synchronous formation of the metamorphic sole and igneous crust of the Semail ophiolite: New constraints on the tectonic evolution during ophiolite formation from high-precision U–Pb zircon geochronology. *Earth Planet. Sc. Lett.*, 451, 185–195. doi:10.1016/j.epsl.2016.06.051. 2016.

20 Rybacki, E., and Dresen, G. Deformation mechanism maps for feldspar rocks. *Tectonophysics*, 382, 173–187. doi:10.1016/j.tecto.2004.01.006. 2004.

Schmidt, N.-H., and Olesen, N. Computer-aided determination of crystal-lattice orientation from electron-channeling patterns in the SEM. *Can. Mineral.*, 27, 15–22. 1989.

Shelley, D. Spider texture and amphibole preferred orientations. *J. Struct. Geology*, 16, 709–717. doi:10.1016/0191-25 8141(94)90120-1. 1994.

Siegesmund, S., Helming, K., and Kruse, R. Complete texture analysis of a deformed amphibolite: comparison between neutron diffraction and U-stage data. *J. Struct. Geology*, 16, 131–142. doi:10.1016/0191-8141(94)90024-8. 1994.

Soret, M., Agard, P., Dubacq, B., Vitale-Brovarone, A., Monié, P., Chauvet, A., Whitechurch, H., Villemant, B. Strain 30 localization and fluid infiltration in the mantle wedge during subduction initiation: Evidence from the base of the New Caledonia ophiolite. *Lithos*, 244, 1–19. doi:10.1016/j.lithos.2015.11.022. 2016.

Soret, M., Agard, P., Dubacq, B., Plunder, A., and Yamato, P. Petrological evidence for stepwise accretion of metamorphic soles during subduction infancy (Semail ophiolite, Oman and UAE). *J. Metamorph. Geol.*, 35, 1050–1080. doi:10.1111/jmg.12267. 2017.

Tatham, D. J., Lloyd, G. E., Butler, R. W. H., and Casey, M. Amphibole and lower crustal seismic properties. *Earth Planet. Sc. Lett.*, 267, 118–128. doi:10.1016/j.epsl.2007.11.042. 2008.

Wakabayashi, J., and Dilek, Y. Spatial and temporal relationships between ophiolites and their metamorphic soles: A test of models of forearc ophiolite genesis. *Geol. Soc. Am. Spec. Publ.*, 349, 53–64. doi:10.1130/0-8137-2349-3.53. 2000.

5 Wakabayashi, J., and Dilek, Y. (2003). What constitutes “emplacement” of an ophiolite?: Mechanisms and relationship to subduction initiation and formation of metamorphic soles. *Geol. Soc. Am. Spec. Publ.*, 218, 427–447. doi:10.1144/GSL.SP.2003.218.01.22. 2003.

Wenk, H. R., and Christie, J. M. Comments on the interpretation of deformation textures in rocks. *J. Struct. Geology*, 13, 1091–1110. doi:10.1016/0191-8141(91)90071-P. 1991.

10 Wheeler, J., Prior, D., Jiang, Z., Spiess, R., and Trimby, P. The petrological significance of misorientations between grains. *Contrib. Mineral. Petr.*, 141, 109–124. doi:10.1007/s004100000225.

Whitney, D. L., and Evans, B. W. Abbreviations for names of rock-forming minerals. *Am. Min.*, 95, 185–187. doi:10.2138/am.2010.3371. 2010.

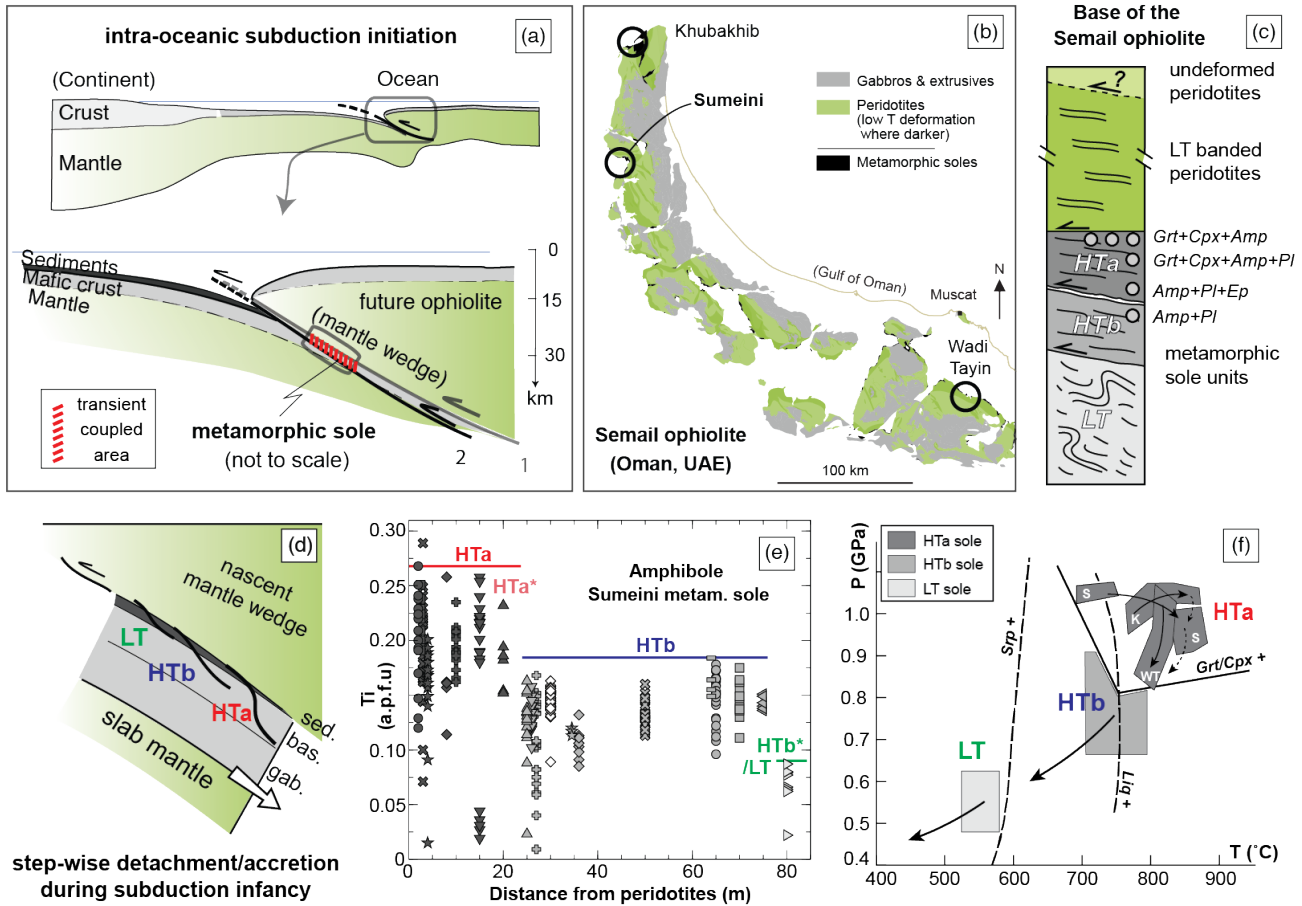


Figure 1: (a) Geodynamic setting of metamorphic sole formation during intra-oceanic subduction infancy (modified after Agard et al., 2016); (b) Simplified geological map of the Semail ophiolite, highlighting the outcrops of metamorphic sole beneath the ophiolite mantle (modified after Nicolas et al., 2000); (c) schematic log of the base of the Oman ophiolite showing the structural position of the samples from Khubakhib (K), Sumeini (S) and Wadi Tayin (WT). See Table 1 for details; (g) Close-up view on the tectonic configuration along the nascent plate interface, during the formation and exhumation of the HTa, HTb and LT soles until reaching the steady state (sketch modified after Agard et al., 2016 and Soret et al., 2017). s: sediment, b: basalt, g: gabbro, m: mantle peridotite (e) Amphibole Ti vs. Si content in amphibolite samples from Sumeini (after Soret et al., 2017) outlining the discontinuous decrease of T conditions during the exhumation of the HT metamorphic sole; (f) Compilations of P-T estimates and associated P-T paths (after Soret et al., 2017), from the Grt-Cpx amphibolite (HTa), to the Pl-rich amphibolite (HTb) and greenschist facies (LT) metamorphic sole units.

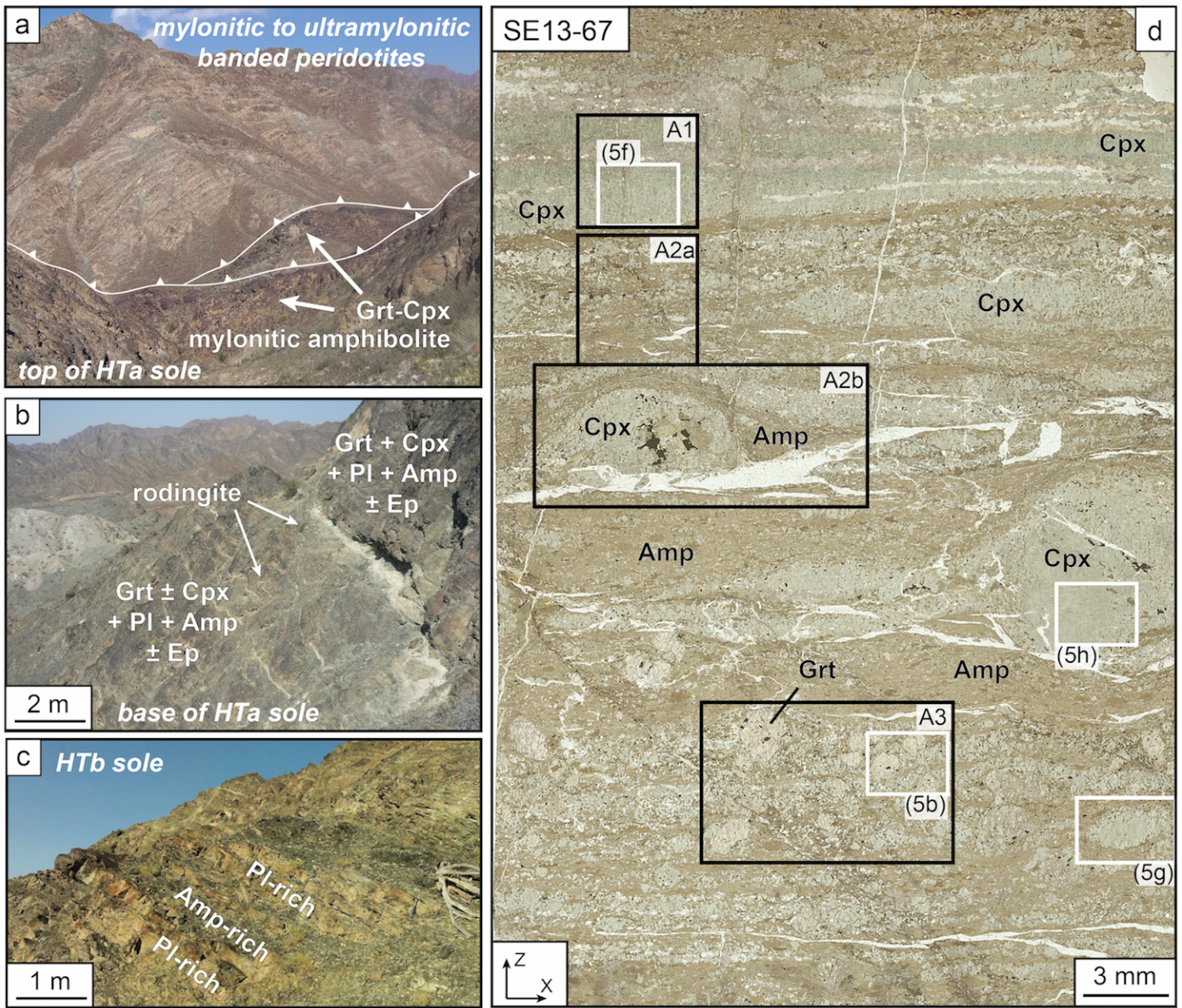


Figure 2: Photographs of the base of the Semail ophiolite outcropping in the Sumeini region (modified after Soret et al., 2017). (a) Basal contact between banded peridotite and the Grt-Cpx amphibolite of the metamorphic sole (zone HTa); (b) base of the HTa unit, widely affected by Ca-rich metasomatism (rodingite); (c) layered structure in zone HTb with alternations from plagioclase-rich to darker amphibole-rich layers; (d-h) Well-preserved mineral equilibrium texture and deformation structure from peak conditions in the HTa amphibolite at Sumeini (~2.5 m from the contact). Black boxes refer to EBSD maps shown in Figs. 3 and 4. White boxes correspond to photographs in Fig. 5.

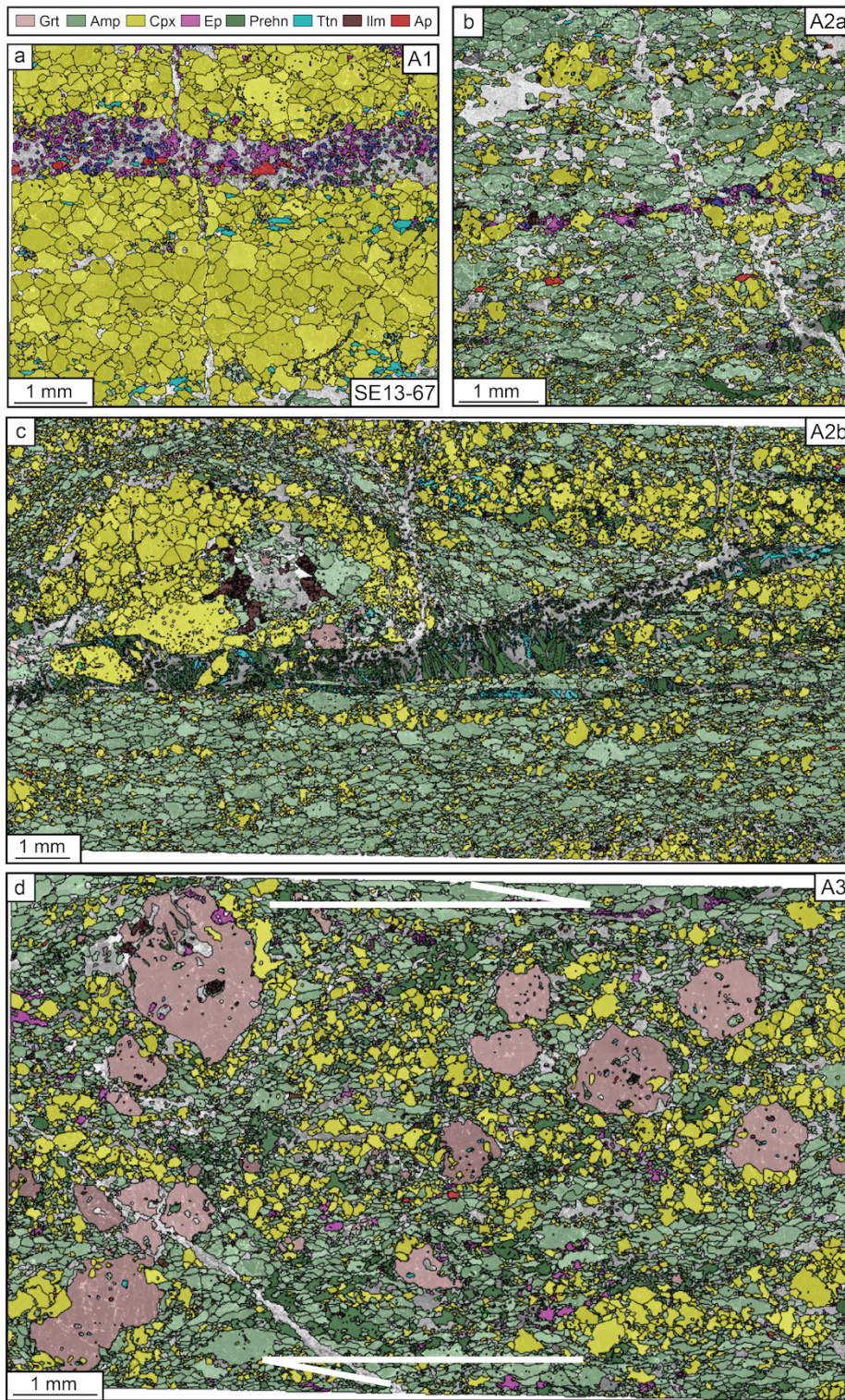


Figure 3: EBSD phase maps from a Grt-Cpx-bearing amphibolite sampled at ~2.5m from the contact with peridotite (sample SE13-67) and showing the best-preserved micro-structures. (a) Area 1 (A1) composed essentially of clinopyroxene with a late vein of epidote; (b) and (c) Area 2 (A2) composed of amphibole and clinopyroxene. (c) A late prehnite vein crosscuts the sample; (d) Area 3 (A3) composed of garnet, amphibole and clinopyroxene.

5

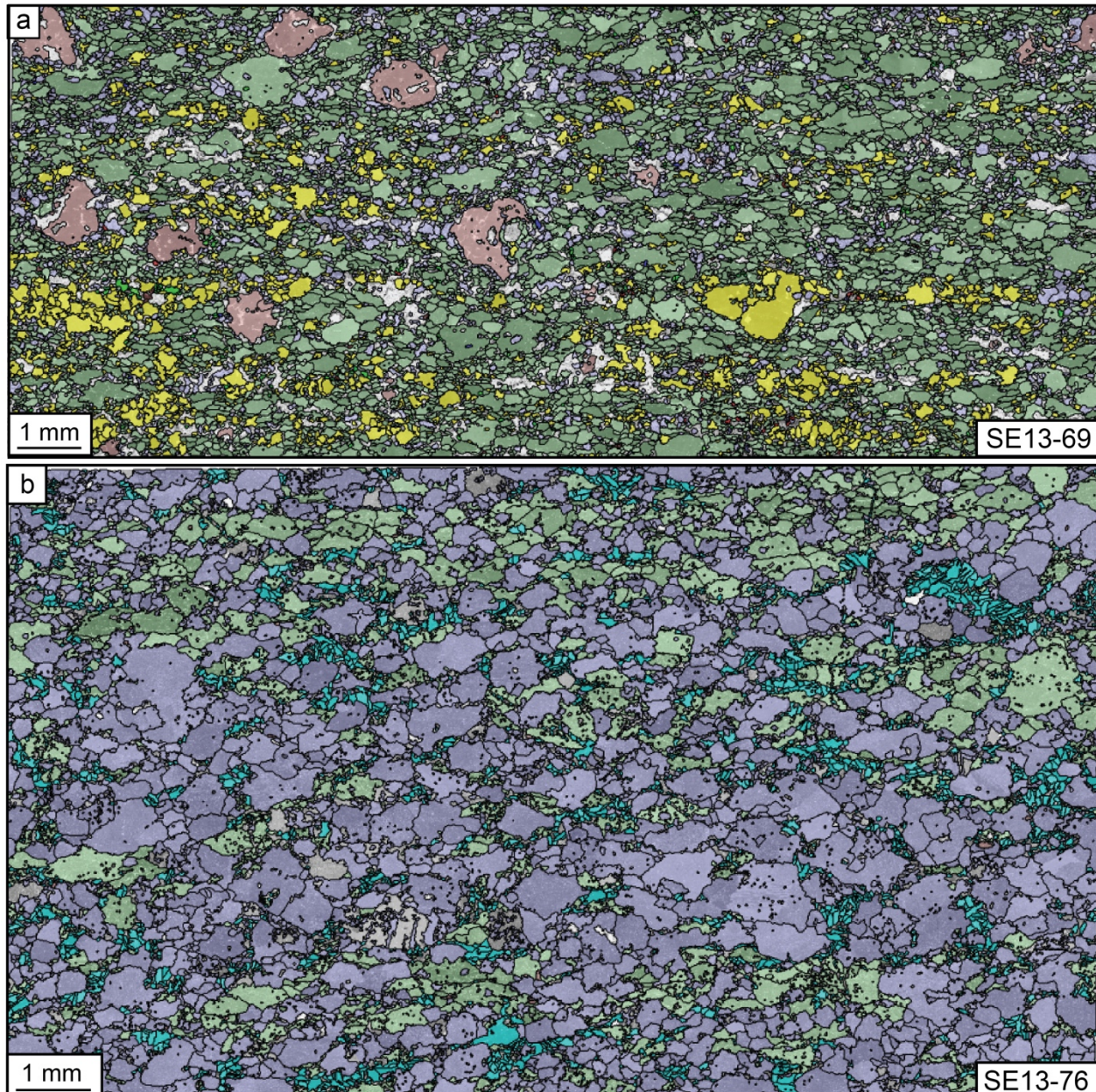


Figure 4: EBSD phase maps (a) from a slightly retrogressed amphibolite facies garnet-clinopyroxene-bearing amphibolite at the top of HTa unit (sample SE13-69; Sumeini area), (b) from a highly retrogressed garnet-clinopyroxene-free amphibolite at the base of HTa unit (sample SE13-76; Sumeini area).

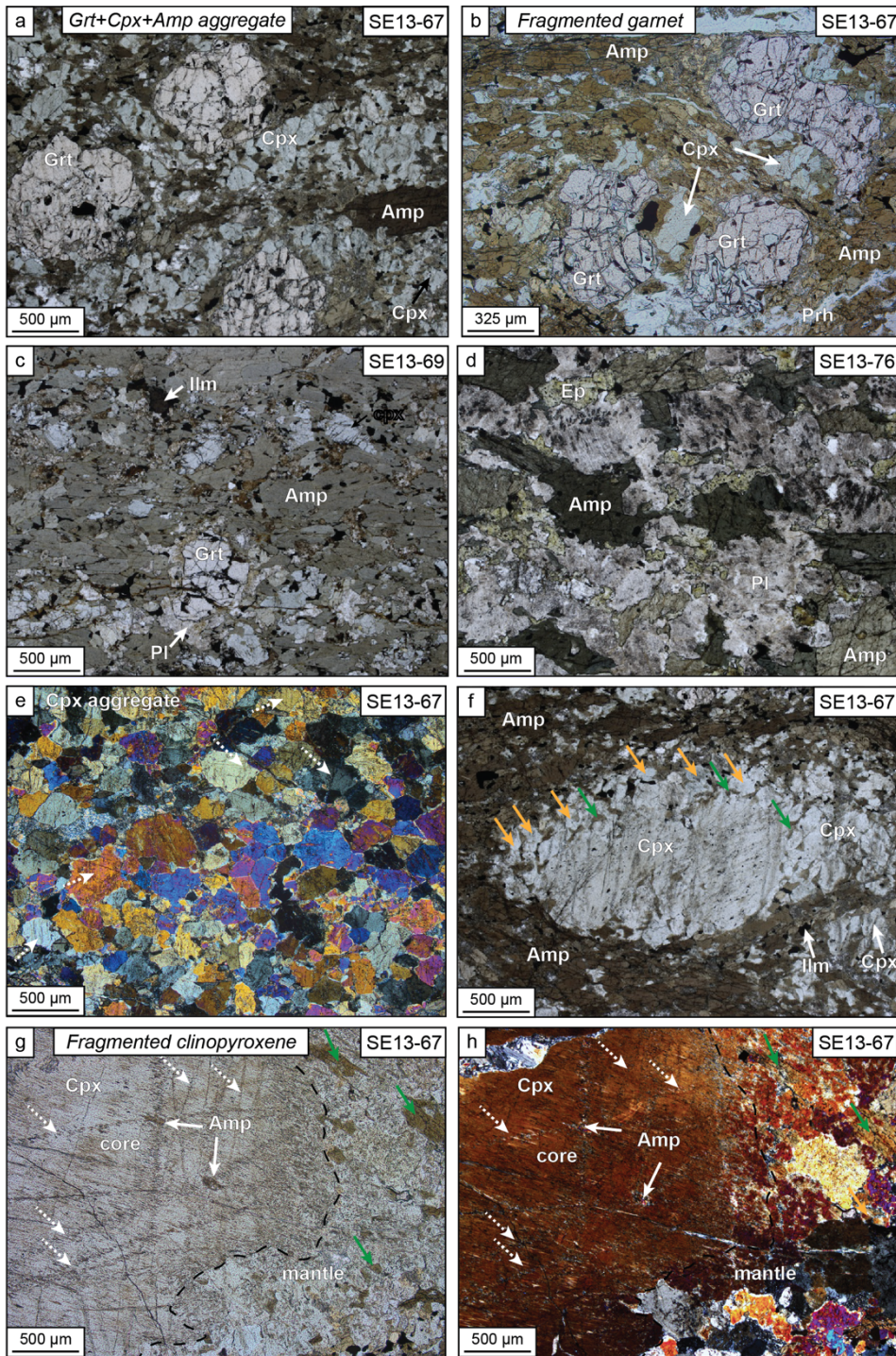


Figure 5: Photographs of representative microstructures in the HTa amphibolites. (a) garnet porphyroclasts surrounded by a fine-grained matrix of Cpx+Amp (Area 3); (b) fractured garnet porphyroblast with fractures filled by a fine-grained matrix composed of Cpx+Amp; (c) ~8 m from the contact, showing greater retrogression characterized by an increase of plagioclase and brown amphibole at the expense of Grt+Cpx; (d) ~25 m from the contact (base of HTa), highly retrogressed amphibolite associated with secondary crystallization of coarse grained brown to green amphibole, epidote and plagioclase; (e) monomineralic layer of recrystallized clinopyroxene by subgrain rotation; (f) sheared Cpx porphyroblast wrapped by fine grained brown Amp (Area 2); (g) and (h; cross polarized light) Core-and-mantle structure in a Cpx porphyroblast with and minute amphibole in sealed micro-fractures (fluid inclusions trails) and at grain boundaries of the porphyroblast mantle. Orange and green arrows point to small new clinopyroxene deriving from the fragmented clinopyroxene porphyroblast and secondary amphibole, respectively. See details in text.

10

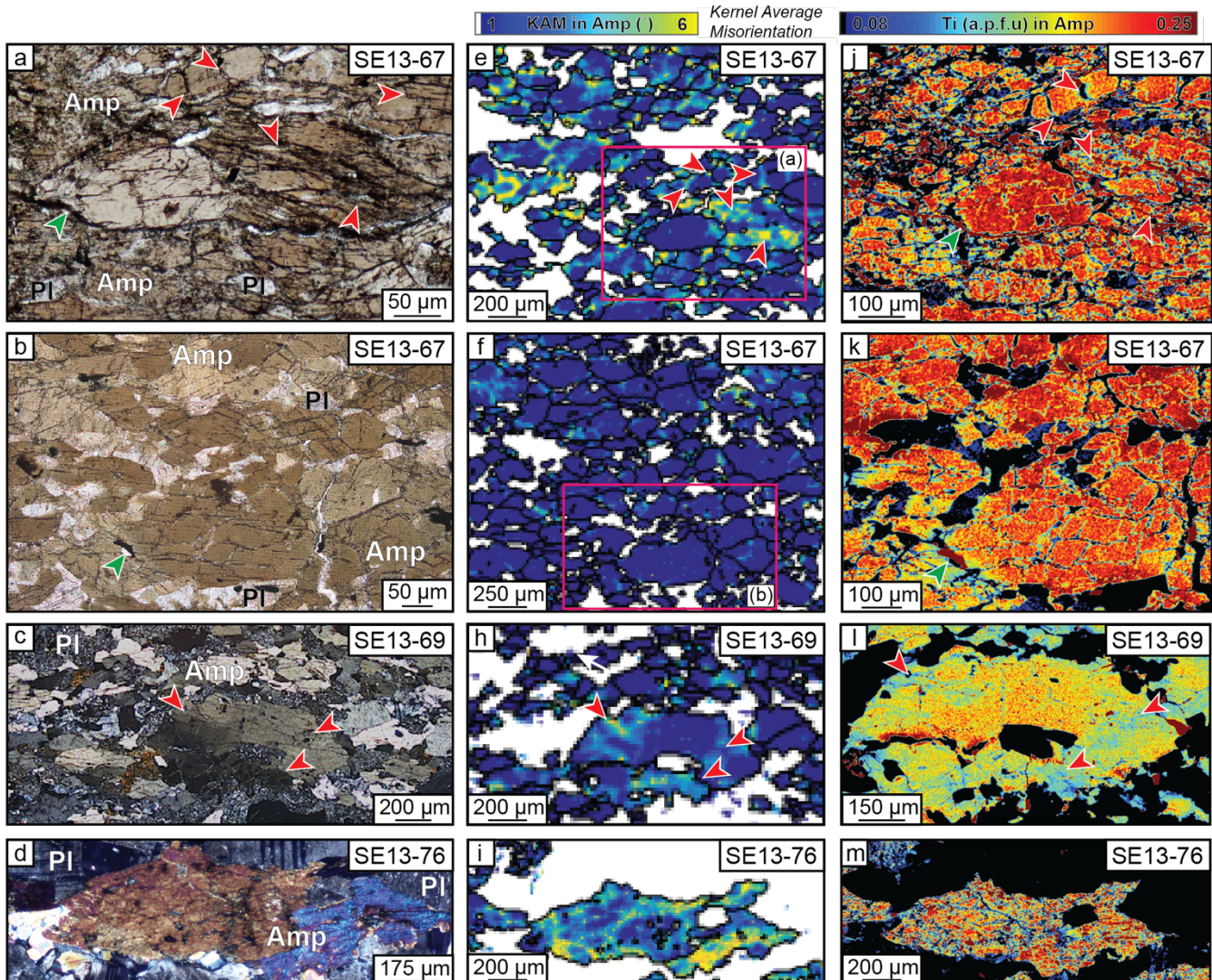


Figure 6: (a-d) Photographs of representative textures of amphibole, (e-i) [2-10°] intracrystalline misorientation (to the mean grain orientation) and (j-m) compositional map of Ti of amphibole in samples sorted in function of the distance from the peridotite. Red and green arrows point to amphibole microfractures and ilmenite veinlets or crystals, respectively.

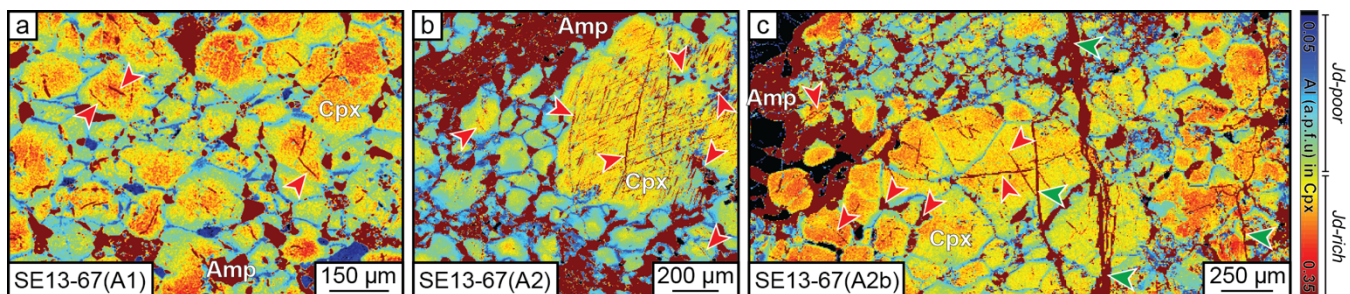
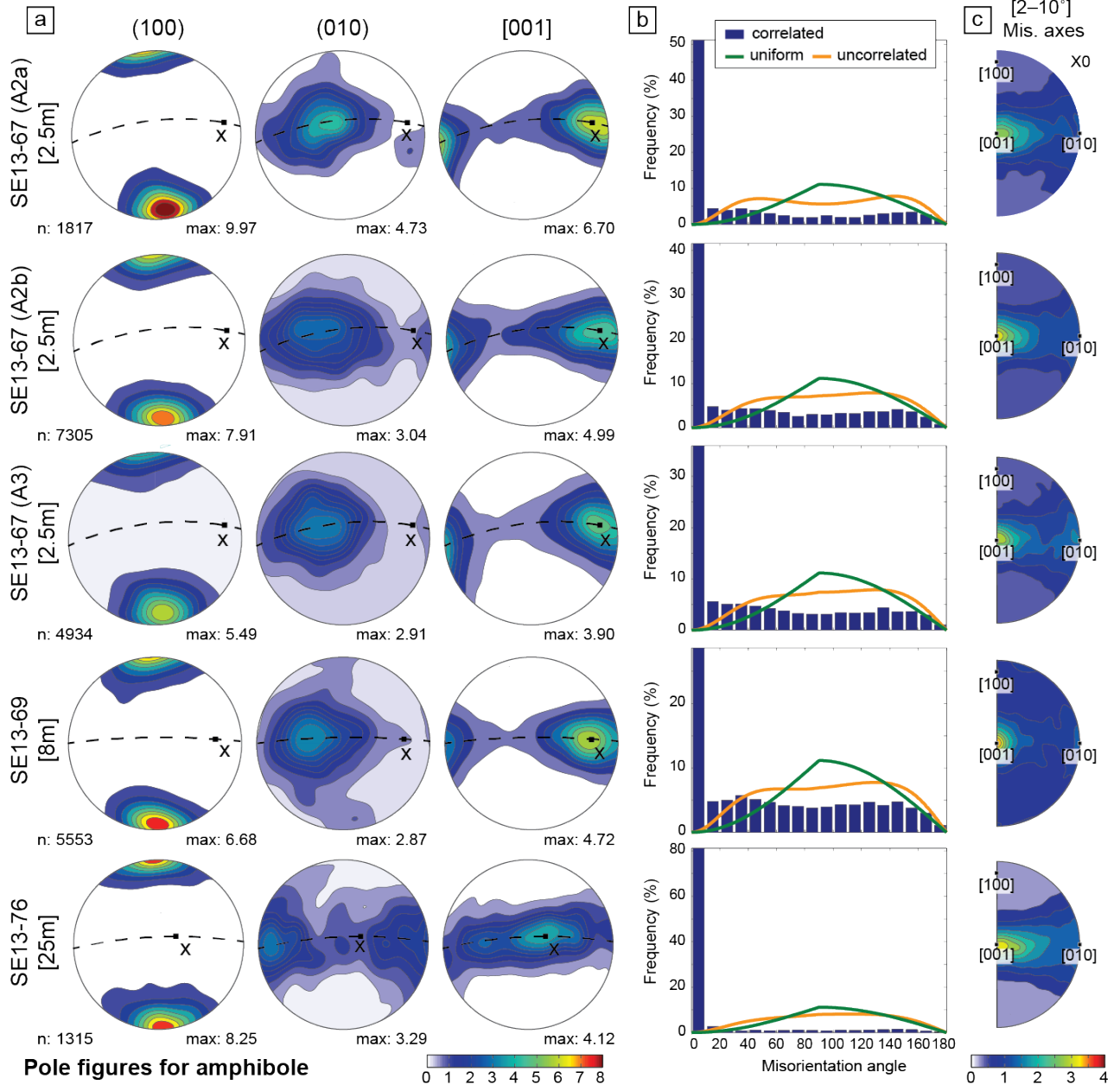


Figure 7: (a) Compositional map of Al of clinopyroxene in mono- and poly-mineralic layers of sample SE13-67. Red arrows points to amphibole in clinopyroxene micro-fractures or in interstitial positions at new clinopyroxene boundaries. Jd: jadeite content. See text for details.



5

Figure 8: (a) Pole figures illustrating amphibole CPO of the samples from the HTa unit in Sumeini massif. Samples are sorted using the distance from the peridotite, with increasing distance downwards. The dashed line represents the foliation and X points to the lineation. Contours are multiples of a uniform distribution. All plots are lower hemisphere projections. Numbers in square brackets refer to the distance to the peridotite. n: number of grains; (b) Distribution of misorientation angles between correlated (adjacent) pixels (blue histogram) and between uncorrelated pixels (orange curve) of amphibole. The uniform (green) curve corresponds to the theoretical misorientation distribution for a perfectly randomly oriented crystals; (c) Amphibole inverse pole figures showing the distribution of correlated misorientation axes (between 2° and 10°). Contours are multiples of uniform distribution.

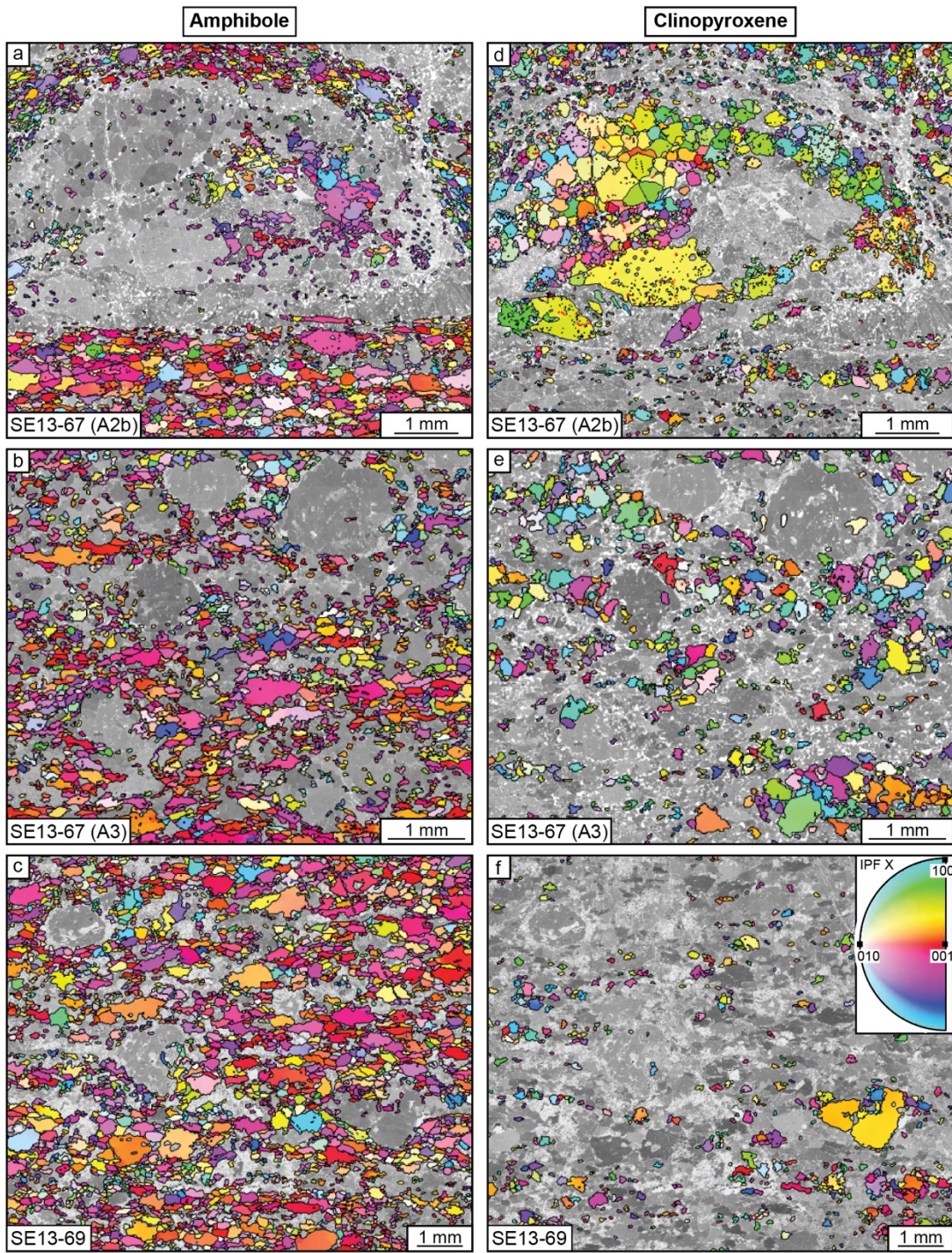


Figure 9: X direction IPF Inverse pole coloring orientation maps for (a-c) amphibole and (d-f) clinopyroxene.

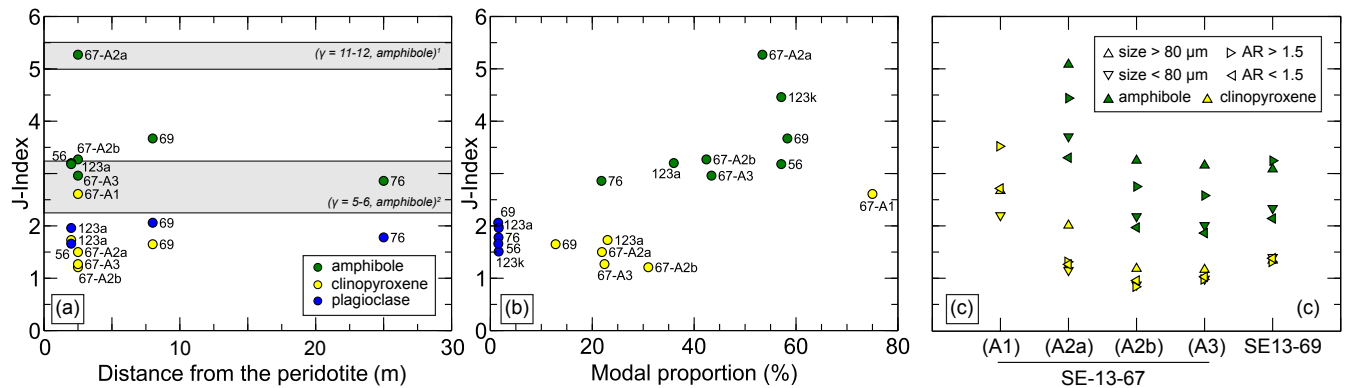


Figure 10: Quantified CPO strength (using the J-index) of amphibole, clinopyroxene and plagioclase vs. (a) the distance from the contact with the peridotite and (b) the modal proportion of each phases from Sumeini, Khubakhib and Wadi Tayin localities (see Table 1); (c) the J-index of amphibole and clinopyroxene in function of their aspect ratio and grain size for the samples from the 5 Sumeini cross-section.

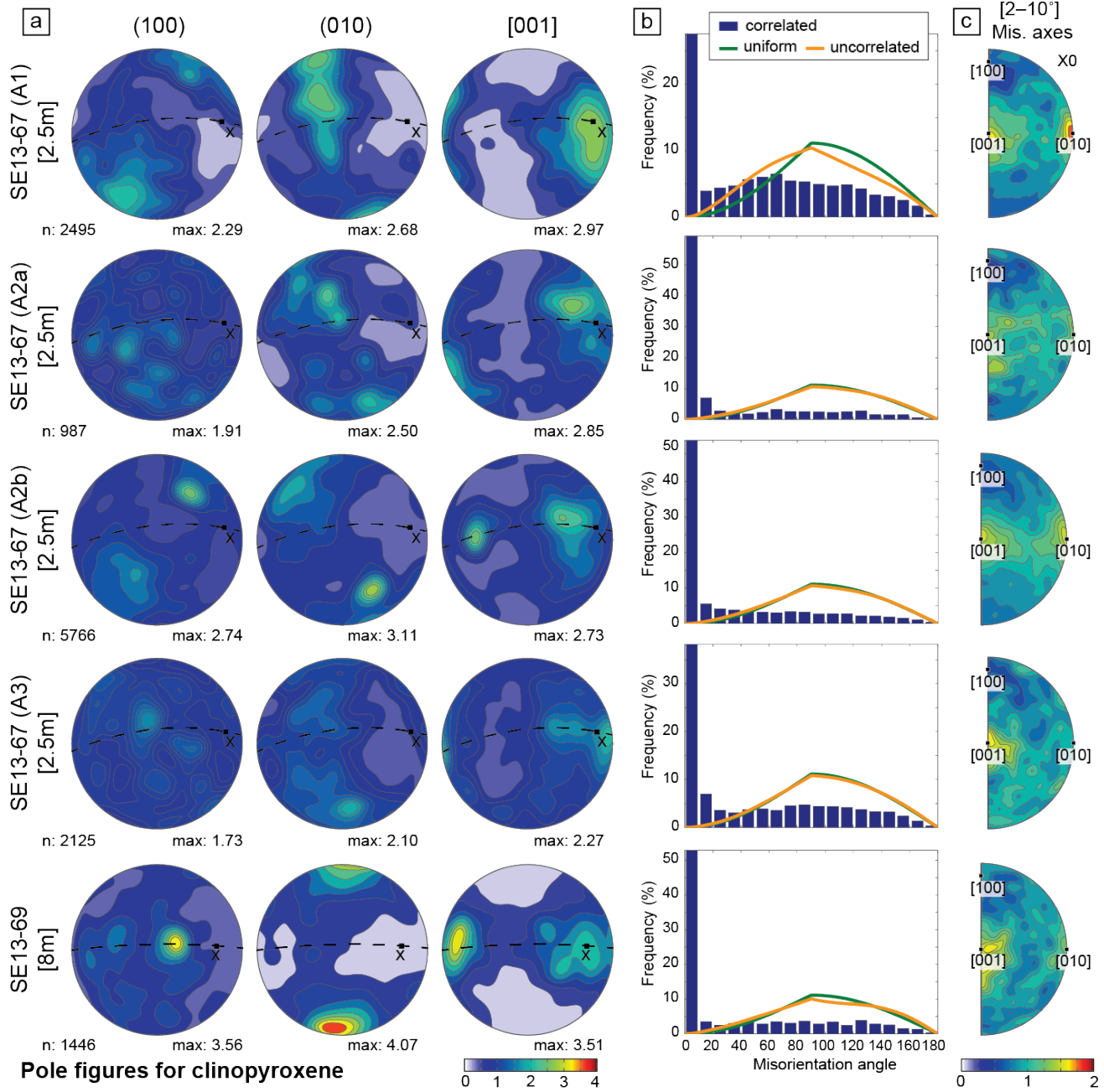


Figure 11: (a) Pole figures illustrating CPO of clinopyroxene in samples from the HTa unit of Sumeini; (b) Distribution of misorientation angles; (c) Inverse pole figures showing the distribution of correlated misorientation axes (between 2° and 10°). See caption of figure 7 for details.

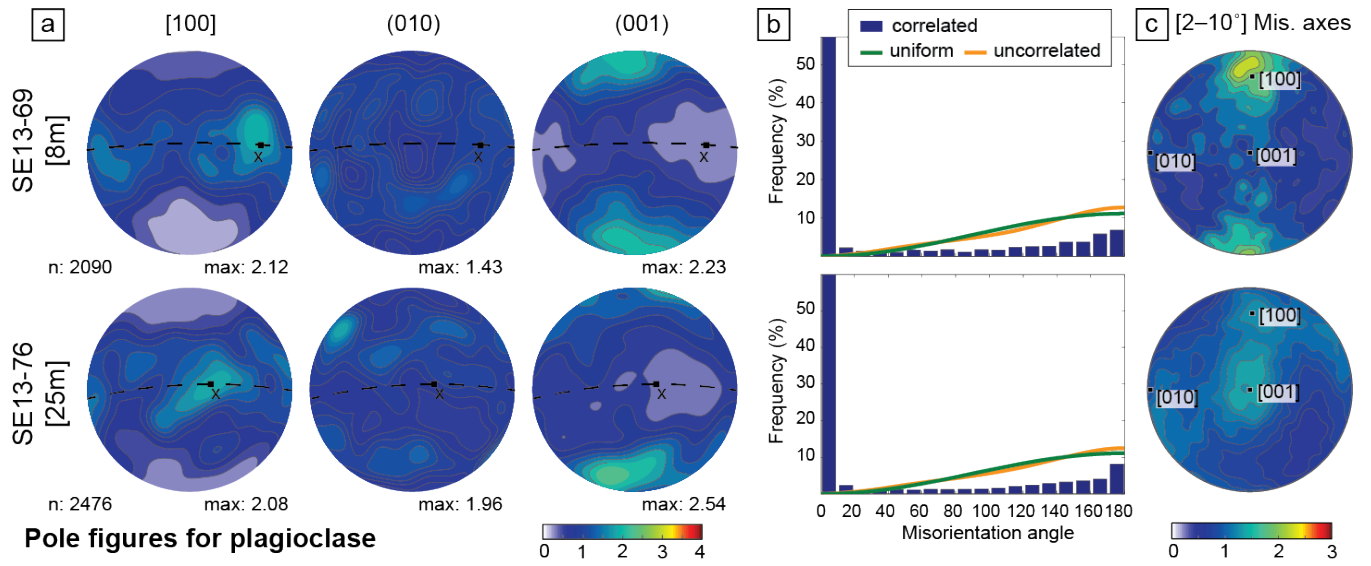


Figure 12: Pole figures illustrating CPO of plagioclase in samples from the HTa unit of Sumeini; (b) Distribution of misorientation angles; (c) Inverse pole figures showing the distribution of correlated misorientation axes (between 2° and 10°). See caption of figure 7 for details. See caption of figure 7 for details.

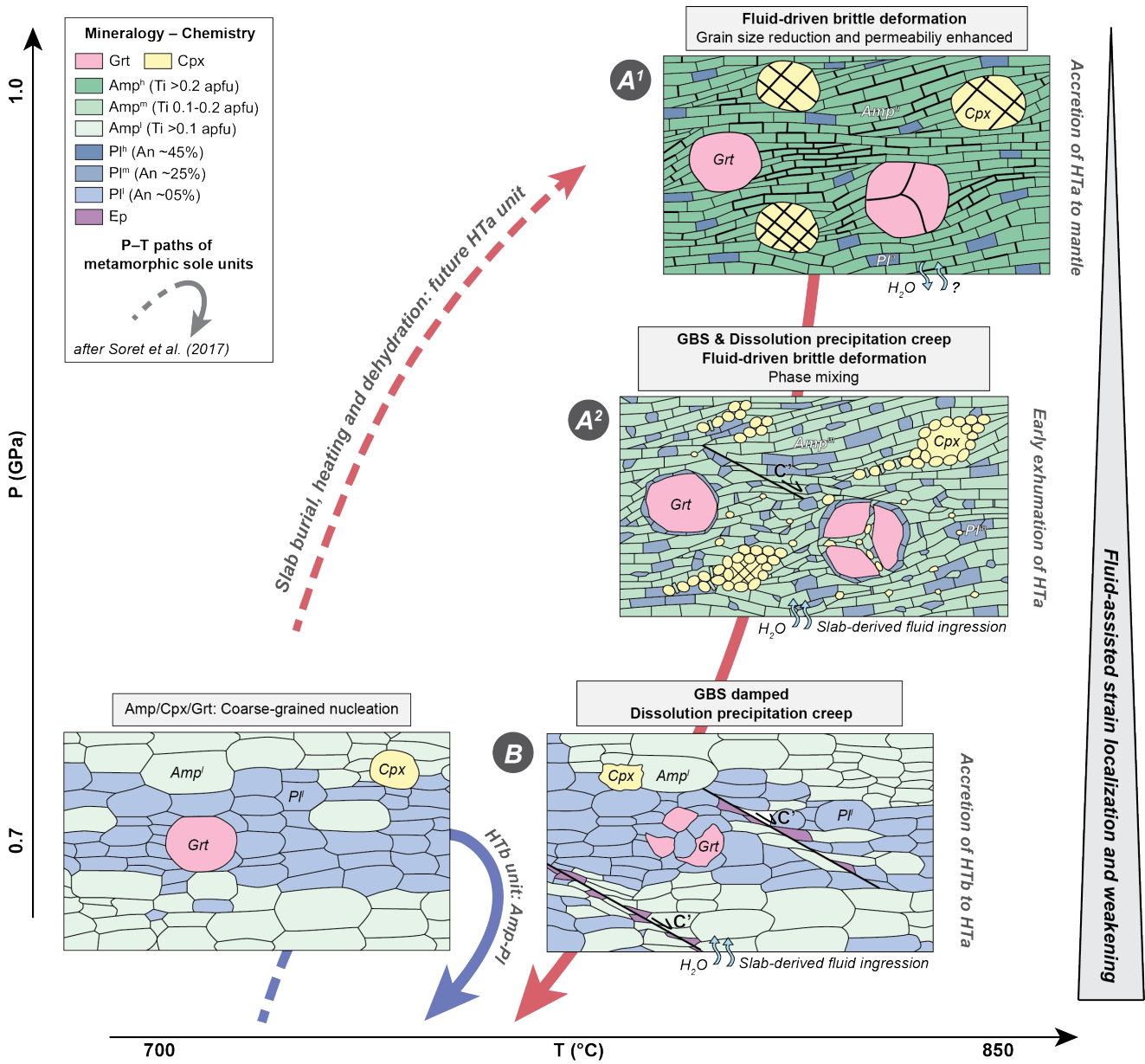
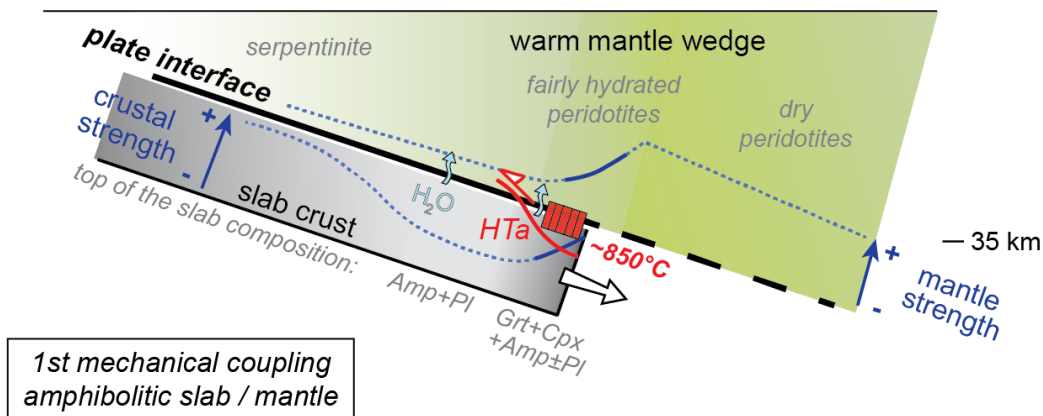


Figure 13: Model evolution at the grain-scale of the deformation of the amphibolite of the Semail metamorphic sole (as a witness of that of the top of the slab crust during subduction infancy) during the formation, accretion and early exhumation to the peridotite during the subduction infancy.

Metamorphic sole (de)formation during subduction infancy

Stage A: (De)formation at 850°C – 1 GPa (HTa accretion)



Stage B: (De)formation at 750°C – 0.7 GPa (HTb accretion)

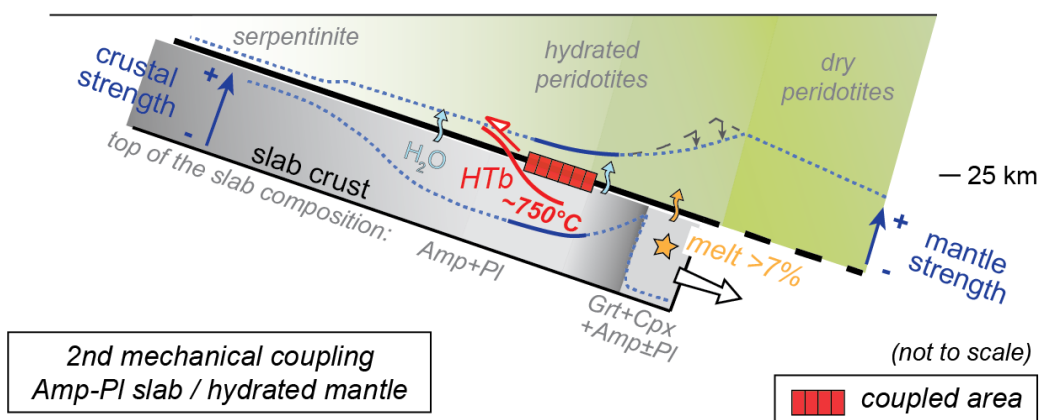


Figure 14: Schematic view of the strength evolution in the top of the slab crust and in the peridotite across the nascent subduction interface. Strong and transient interplate mechanical coupling allows the detachment and accretion of HTa and HTb metamorphic soles units to the peridotite (of the future ophiolite).

Table 1. Sample location, mineral assemblage and micro-structure quantification.

Loc.	Sample (Area)	Dist. (m)	Zone	Pixel length h (μm)	Phase % area					Median grain size (μm)				Mean aspect ratio				J index [M index] (1 point per grain)			Number of map grains (>10 pixels)						
					Grt	Amp	Cpx	Pl	NI	Grt	Amp	Cpx	Pl	Grt	Amp	Cpx	Pl	Amp	Cpx	Pl	Grt	Amp	Cpx	Pl			
Sum.	SE13-67 (A1)	2.5	HTa	8	—	3	75	—	8	—	—	31	—	—	—	1.53	—	—	2.61	—	—	—	2495	—			
	SE13-67 (A2a)	2.5	HTa	8	—	53	22	—	18	—	56	51	—	—	1.89	1.63	—	5.27	1.50	—	—	1817	987	—			
	SE13-67 (A2b)	2.5	HTa	8	—	43	31	—	13	—	57	57	—	—	1.87	1.64	—	3.27	1.21	—	—	7305	5766	—			
	SE13-67 (A3)	2.5	HTa	8	12	42	22	—	13	105	55	57	—	1.47	1.87	1.58	—	0.124	0.011	—	—	50	4934	2125	—		
Khu.	SE13-69	8	HTa	15	3	58	13	14	9	197	93	88	81	1.39	1.81	1.57	1.54	0.114	0.011	—	3.67	1.65	2.06	33	5553	1446	2090
	SE13-76	25	HTa*	15	—	22	—	60	6	—	110	—	124	—	1.90	—	1.60	0.086	—	2.86	—	1.78	—	1315	—	2476	
	SE13-123a	2	HTa	11	7	36	23	17	11	171	68	68	59	1.73	1.96	1.61	1.64	0.113	0.042	0.037	3.20	1.73	1.96	23	2202	1108	1548
WT.	SE13-123k	40	HTb	10	9	57	—	15	6	339	106	—	68	1.49	1.82	—	1.63	0.157	—	4.46	—	1.51	—	89	5793	—	4192
	SE13-56	4	HTa*	12	—	57	4	25	10	—	72	97	62	—	1.86	1.65	1.56	3.18	—	1.66	—	3478	149	2747	[0.115]	[0.031]	—

— : not present; NI: not indexed phase

Sum.: Sumeini; Khu.: Khubakhib; WT.: Wadi Tayin

Table 1.**Table 2.** Deformation evolution of the HTa amphibolite

	A1 - HTa accretion 850°C / 1 GPa (Fig.)				A2 - Early exhumation 850-750°C (Fig.)				B1 - HTb accretion 700-750°C / 0.7 GPa			
	Grt + Cpx + Amph ^h				Amp ^m + Cpx + Pl				Amp ^l + Pl			
Garnet	Fracturing (5b)				Rigid Particule (3d)				Absent or Trace			
Clinopyroxene	Dissolution (5d)				Dynamic recrystallization (5f-h)				Absent or Trace			
Amphibole	Fracturing + healing along specific planes (5g,h)				Dissolution - Precipitation (5c)				Dissolution - Precipitation (5a,c) (S1)			
Plagioclase	Fracturing + healing along specific planes (6a,b) (6j,k)				Brittle Deformation (-) (6c,l)				Dissolution - Precipitation (6b,c)			
Bulk rock amphibolite	Fine-grained nucleation (6b,c)				Dissolution - Precipitation (6d)				Dissolution - Precipitation (6d)			
Strain	Grain Size Reduction (3a-d)				Phase Mixing (3a-d)				Rock re-equilibration			
	Fluid-assisted brittle deformation				GBS - diffusion creep (3d) (4a)				GBS damped - diffusion creep			
	Fluid-assisted strain accommodation and weakening											

Table 2.

Supplementary material:

Figure S1: EBSD maps from (b) a well-preserved Grt-Cpx amphibolite from the top of a HTa unit (sample SE13-123a; Khubakhib); (b) a well-preserved plagioclase-rich amphibolite at the top of a HTb unit (sample SE13-123k; Khubakhib); (c)

5 a slightly retrogressed at amphibolite facies clinopyroxene-bearing amphibolite at the top of a HTa unit (sample SE13-57; Wadi Tayin). See Table 1 for details.

Figure S2: Long axis orientation, grain size and aspect ratio of amphibole (a-c) and clinopyroxene (d-f). (a) and (d): Shape-preferred orientation (SPO) vs. grain size; (b) and (e) SPO vs. aspect ratio; (c) and (f) grain size vs. aspect ratio. The longest line represents the shear plane. The two smaller lines are placed at 60 and 120° and outline the data dispersion.

10 **Figure S3:** Pole figures illustrating CPO of plagioclase in samples from the HTa unit of Wadi Tayin, and HTb unit of Khubakhib. See Table 1 and caption of figure 7 for details.

Figure S4: Pole figures illustrating CPO of amphibole and clinopyroxene samples from the HTa unit of Wadi Tayin, and HTb unit of Khubakhib. See Table 1 and caption of figure 7 for details.

15 **Figure S5:** X direction IPF Inverse pole coloring orientation maps for (a) amphibole and (b) clinopyroxene and (d) plagioclase of samples from the HTa unit in Sumeini.